Reflection of Storm Surge and Tides in Convergent Estuaries with Dams, the case of Charleston, USA

Steven L. Dykstra[1,2,3*], Enrica Viparelli[3], Stefan A. Talke[4], Alexander E. Yankovsky[2], Raymond Torres[2]

[1]College of Fisheries and Ocean Science, University of Alaska Fairbanks, Fairbanks, AK 99775.

[2]School of Earth, Ocean, and Environment, University of South Carolina, Columbia, SC 29208.

[3]Department of Civil and Environmental Engineering, University of South Carolina, Columbia, SC 29208.

[4]Department of Civil and Environmental Engineering, California Polytechnic State University, San Luis Obispo, CA 93407.

Corresponding Author: Steven L. Dykstra (sdykstra@alaska.edu)

Key Points:

- Estuarine water levels are predicted from amplitudes and phases of interrelated incident, partially reflected, and fully reflected waves
- Three convergence regimes emerge: dominant tides have near peak amplification, overtides attenuate, and long duration surges mildly amplify
- Dams reflect and amplify long waves—increasing flood exposure—the most in weakly convergent estuaries

Key Words: Long Waves, Estuary, Storm Surge, Coastal Flooding, Dam, Convergence, Tidal Dynamics, Partial Reflection

Abstract

Convergent coastal-plain estuaries have been shortened by dam-like structures worldwide. We used 31 long-term water level stations and a semi-analytical tide model to investigate the influence of a dam and landward-funneling on tides and storm surge propagation in the greater Charleston Harbor region, South Carolina, where three rivers meet: the Ashley, Cooper, and Wando. Our analysis shows that the principle tidal harmonic (M2), storm surge, and long-period setup-setdown (~4–10 days) propagate as long waves with the greatest amplification and celerity observed in the M2 wave. All waves attenuate in landward regions, but, as they approach the dam on the Cooper River, a frequency dependent response in amplitude and phase progression occurs. Dam-induced amplification scales with wave frequency, causing the greatest amplification in M2 overtides. Model results show that funneling and the presence of a dam amplify tidal waves through partial and full reflection, respectively. The different phase progression of these reflected waves, however, can ultimately reduce the total wave amplification. We use a friction-convergence parameter space to demonstrate how amplification is largest for partial reflection, when funneling and wave periods are not extreme (often the case of dominant tides), and for full reflection, when funneling and/or wave periods are small. The analysis also shows that in the case of long period events (>day), such as storm surges, dams may attenuate the wave in funneling estuaries. However, dams may amplify the most intense storm surges (short, high) more than funneling with unexpected consequence that can greatly increase flood exposure.

Plain Language Summary (<=200 words)

Most ports and mega cities are located along estuaries and deltas where flood hazards are increasing primarily due to human modifications of channels and sea level rise. Dams, salt barrages, and surge barriers are common in estuaries. They can modify estuarine geometry, regulate seaward river flow, protect from flooding during storms, and prevent salt intrusion. Many estuaries are naturally convergent, wide near the sea and narrower landward. However, dams form a barrier which shortens an estuary. Like ocean swell at a seawall, tides reflect off dams and often increase tidal range. Here we investigate how dams influence tides and storm surges. Using measurements from the greater Charleston Harbor, we find that constructing a dam can elevate or reduce water levels, depending primarily on estuary convergence and event

duration, as well as flow resistance and river flow. Dams increase flood exposure the most when convergence is weak and when storm surge at the sea has a short duration and high water levels. The analysis also suggests that channelization, such as the proposed dredging of Charleston Harbor, increases the magnitude and seaward extent of dam effects with increasing flood risks.

1 Introduction

Tidal amplitude and probability of coastal flooding has changed over time in estuaries and deltas because of dredging, navigational infrastructure development, land reclamation, and other local geomorphic changes (e.g., Bosserelle et al., 2022; Dijkstra et al., 2019; Ralston 2022; Winterwerp et al., 2013; Talke et al., 2014; Ralston et al., 2019; Orton et al., 2020; de Leo et al., 2022). Geometric changes in estuaries and deltas also alter currents and mixing—disrupting the morphodynamic equilibrium—which shifts locations of erosion and deposition. The net change in bathymetry feeds back into the effective frictional damping, resonance, and reflection acting on the tides (e.g., Chernetsky et al., 2010; Familkhali et al., 2020; Talke & Jay 2020). Additionally, nonlinear interaction between river discharge and tides is altered as bathymetry is changed (Godin, 1999; Kukulka & Jay, 2003; Buschmann et al., 2009; Talke et al., 2021). Net bathymetric changes and how they interact with river flow and tides can modify tidal datums—such as Mean High Water (MHW) and the Mean Water Level (MWL)—over decadal time scales (e.g., Jay et al., 2011; Helaire et al, 2019; Ralston et al., 2019; Talke et al. 2021). If sea level rise deepens estuaries, additional changes in tidal magnitude may further increase high water levels (Lee et al., 2017). Bathymetric changes caused by natural processes, anthropogenic development, and sea-level rise likely influence the dynamics of other types of waves, including storm surge and river floods (e.g., Dykstra & Dzwonkowski, 2020, 2021; Familkhalili et al., 2022) along with seiches, meteotsunamis, and edge waves (e.g., Zhang & Yankovsky et al., 2016).

Some of the most dramatic shifts in tidal properties over the past 150 years have occurred due to tidal reflection off a dam (Winterwerp et al., 2013; Talke & Jay, 2020). For example, reflection from dams on the Hudson River (New York) and Tombigbee River (Alabama)—both ~250 km inland—amplify tides to the same tidal range as the estuary mouth (Dykstra et al., 2022; Georgas, 2012; Ralston et al., 2019). The Ems Estuary, Netherlands/Germany, was shortened with a dam in 1899 and then channelized. These changes increased the tidal range up to five-fold, dramatically altering the estuary regime with strong landward sediment transport that now fills the port with fluid muds (e.g., SSC>10kg m^{-3}; Chernetsky et al., 2010; Dijkstra et al., 2019; Talke et al. 2009; Talke & Jay, 2013; Winterwerp et al., 2013). In contrast, estuaries with natural reflection points are relatively stable (e.g., James, Potomac, Connecticut Rivers) and

suggest the sudden changes following dam construction may force estuaries to a new morphodynamic equilibrium (Figueroa et al., 2022).

Dams in coastal channels influence tidal currents—altering sediment transport, salinity intrusion and biogeochemical cycling (Arunpandi et al., 2022; Díez-Minguito et al., 2012; Kidd et al. 2017; Figueroa et al., 2022)—and may affect storm surges, altering flooding dynamics. These dams are extensively dispersed, from tropical to polar estuaries (e.g., river dams, weirs, locks, sluice gates; Arunpandi et al., 2022; Kyzyk et al. 2008; Webster et al. 2010). China alone has over 320 so-called *salt barrages*, built to reduce salt intrusion from dredging and sea level rise (Tilai et al., 2019). As marine influences continue to extend inland due to channel dredging, and as sea-level rise spurs the development of protection barriers, the magnitude and number of dam-marine interactions will likely increase. However, documented in-situ observations of the influence of dams on storm surge and extreme water levels are limited (Orton et al., 2023). On the Tombigbee River (Alabama), dam-induced tidal amplification—when river discharge is low—may be damped by high river discharge (Dykstra et al. 2022). However, because some storm surge can still reach the dam, water levels are increased and flood duration is longer than in the case of a river or coastal flood alone (Dykstra & Dzwonkowski, 2021). In this contribution, we investigate how dam construction and flow regulation have influenced tides, storm surge, and high water levels in the naturally convergent channels of the Charleston estuary, South Carolina. Because storm surge, tides, and other long period waves (period of hours to days) are shallow water waves in estuaries (wave length>>depth), we use the tools of analytical tidal theory to gain insights into the dynamics of these other waves.

Field observations suggest that dams primarily affect tides through reflection (Díez-Minguito et al., 2012). Here, we also investigate how shortening an estuary may influence long wave dynamics from overtides to setup-setdown (storm surge is later defined statistically as a large amplitude setup event), in naturally convergent and modified systems. We analyze long term water level observations from 31 stations in the Charleston estuary, South Carolina, USA, where we compare long wave propagation on the dammed Cooper River to the undammed Ashley and Wando rivers. After differentiating the incident and reflected long wave components observationally, we employ a semi-analytical one-dimensional model to further demonstrate the effects of landward channel funneling, which is then expanded to show broad applications in a

friction-convergence parameter space. The primary scientific contributions of this study are developing mechanistic understandings of long waves—beyond tides—in 1) convergent estuary channels and 2) all estuaries with dams.

2 Background Information and Theory on Convergence and Friction in Estuaries

2.1 Full and Partial Wave Reflection

In idealized, naturally convergent systems, alluvial estuaries reach morphodynamic equilibrium through the influence of tidal energy in a balance of exponential landward funneling, which generates partial reflections and amplifies tides, and friction, which attenuates tides (Fredrichs & Aubrey, 1994; Friedrichs et al., 1998; Jay et al., 1991; Schuttelaars & de Swart, 2000; Wright et al., 1973). More generally, partial reflections occur to enforce continuity in tidal discharge and tidal amplitude anytime the phase speed c or cross-sectional area changes, which can occur due to changes in width, depth, or frictional effects (e.g., bottom roughness; Battjes & Labuer, 2014; Dronkers, 1964). Thus, for a coordinate system in which $x=0$ at the coast and increases landward, the general solution for a long wave in an estuary contains both an incident and a reflected wave:

$$\eta(x,t) = \underbrace{A\cos(\omega t + kx)}_{Reflected\ Wave} + \underbrace{B\cos(\omega t - kx)}_{Incident\ Wave} = Re\left[\left(\underbrace{Ae^{kx}}_{Reflected\ Wave} + \underbrace{Be^{-kx}}_{Incident\ Wave}\right)e^{i\omega t}\right], \#(Equation\ 1)$$

where $k=\frac{2\pi}{\lambda}$ is the wavenumber (λ is wavelength), $\omega=\frac{2\pi}{T}$ is the angular frequency (T is tidal wave period), A and B are amplitudes at x=0 and Re denotes the real term. The terms ωt and kx together constitute the phase φ (e.g., $\varphi=\omega t–kx$) which—in the landward direction—decreases for the incident wave and increases for the reflected wave. At a barrier with a no flux condition, a fully reflected wave with a phase shift of zero degrees occurs and constructively interferes with the incoming wave (i.e., $0^\circ\sim\varphi_r–\varphi_i$, where the subscripts r and i represent the reflected and incident waves, respectively). The reflected wave attenuates due to friction and as cross-sectional area diverges in the seaward direction, where the propagating wave becomes progressively less in-phase with the incoming wave (i.e., $0^\circ<|\varphi_r–\varphi_i|<90^\circ$). Hence, constructive interference is most prominent near the reflected boundary (e.g., Chernetsky et al., 2010). At a location of partial reflection, the amplitude of the reflected wave is often small compared to the incident wave that continues (i.e., transmitted wave), provided the geometric or wavenumber change is small and phase speeds are similar (Battjes & Labuer, 2014). The net phase difference

between the incident and reflected wave depends on the sum of all the reflections throughout the estuary, leading to a reflected wave with a phase—relative to the incident wave—of –π to π. Hence, because partial reflections are distributed throughout a convergent estuary, their net effects contribute to the resulting wave amplitude and net phase progression.

In an estuary with convergence and reflection from a dam, both total and partial reflection effects are present. With time and distance from a location of full reflection, the phase difference increases, leading to destructive interference when the incident and reflected waves become out-of-phase (i.e., $90^\circ<|\varphi_r-\varphi_i|<270^\circ$), resulting in a smaller overall amplitude. For funneling estuaries, partial reflection and frictional damping affect incident tides everywhere. Landward funneling makes partial reflection effects cumulative. In contrast, dams induce full reflection (i.e., no transmission) at a single location, generating a fully reflected wave that propagates seaward along with the partially reflected waves generated by funneling.

2.2 Theoretical Friction-Convergence Relationships

The convergence parameter Δ is a non-dimensional measure of funneling for an idealized estuary of mean depth *h* and exponentially decreasing area *a* in the landward direction (Jay, 1991):

$$\Delta = \frac{\sqrt{gh}}{2L_a\omega} = \frac{1}{4\pi}\frac{\lambda}{L_a}, \#(Equation\ 2)$$

where *g* is gravitational acceleration. The e-folding length of cross-sectional area L_a determines the funneling rate $1/L_a$ and is found by fitting the area to $a(x) = a_0 e^{-x/L_a}$, where a_0 is cross-sectional area at the mouth. The parameter Δ captures the relationship of wavelength (or wavenumber; i.e., $\Delta = \frac{1}{2}k^{-1}L_a^{-1}$) and geomorphic funneling and implies that convergence effects have an inverse relationship with L_a and scale with wave period. In comparison, frictional effects *r*, which depend on the square of tidal velocity U_t, can be linearized as:

$$r = \frac{8}{3\pi}\frac{C_d U_t}{h}, \#(Equation\ 3)$$

where C_d is the drag coefficient. The parameter *r* scales with the tidal velocity-depth ratio and is made non-dimensional by dividing by ω (i.e., $\frac{r}{\omega}$).

When funneling and frictional effects in the shallow water wave equations balance (i.e., in an *ideal* or *synchronous estuary*), the tidal amplitude in the landward direction is nearly constant and in a condition called *critical convergence* (Δ_C). This condition is said to occur at

$\Delta_C \approx 1$ and is the basis for simplifying equations, explaining tidal dynamics, and delineating estuaries as strongly convergent when $2\Delta \sim 1$ or weakly convergent when $2\Delta \ll 1$ (Friedrichs, 2010; Lanzoni & Seminara, 1998). A likewise frictional delineation is made for strongly dissipative ($\frac{r}{\omega} \gg 1$) and weakly dissipative estuaries ($\frac{r}{\omega} \ll 1$; e.g., Lanzoni & Seminara, 1998). Estuarine tidal waves are often at or below critical convergence, for which the dynamics of weakly convergent-strongly dissipative estuaries are commonly assumed and simplified to a single incident wave with the rate of frictional decay offset by a constant funneling rate (see Friedrichs, 2010; c.f. Jay, 1991; Lanzoni & Seminara, 1998; van Rijn, 2011; Savenije et al., 2008).

While tides are astronomically forced with defined frequencies (i.e., harmonics), setup-setdown is atmospherically forced (e.g., wind, barometric pressure) and commonly has a longer period with large ranges, forming the so-called *weather frequency band* (e.g., 1–10 days). On continental shelves, tides are inertial-gravity waves and setup-setdowns are vorticity waves, but in confined river channels both propagate as remotely forced long gravity waves (Yankovsky & Iyer, 2015), suggesting estuarine tidal theory can be applied to long waves in the weather frequency band (Famikhalili et al., 2020; Proudman, 1955; Spicer et al., 2019). By the above definitions, these waves can be strongly or weakly convergent, strongly or weakly dissipative, and vary from event to event. While applicable theory is derived to model weather frequency band estuarine waves (e.g., Jay, 1991; Friedrich & Aubrey, 1994; Toffolon & Saveneije, 2011), a physical explanation of the solutions and applicable conditions are not understood (Winterwerp & Wang; 2011).

We broaden explanations and constrain conditions of analytical tide models by confining approximate convergence and dissipation delineations based on wave properties. When the wavenumber $k_0 = \frac{2\pi}{\lambda}$ of a long wave is affected by acceleration and friction (k_f; Dronkers, 1964) or acceleration, friction, and convergence (k_j; Jay, 1991):

$$k_0 = \frac{\omega}{\sqrt{gh}}, \#(Equation\ 4.1)$$

$$k_f = \frac{\omega}{\sqrt{gh}} \sqrt{-1 + i\frac{r}{\omega}}, \#(Equation\ 4.2)$$

$$k_j = \frac{\omega}{\sqrt{gh}} \sqrt{-(\underbrace{1}_{acceleration} - \underbrace{\Delta^2}_{convergence}) + \underbrace{i\frac{r}{\omega}}_{friction}}. \#(Equation\ 4.3)$$

These terms show that friction makes the wavenumber complex and acts to increase the wavenumber (i.e., decrease wavelength and amplitude) while convergence is a real term—which modifies acceleration (i.e., *1*)—and can further *increase* or *decrease* the wavenumber. As the wavenumber approaches zero, wavelength becomes infinity long, the phase stops progressing landward, and a standing wave forms. In Equation 1, the incident and reflected wave amplitudes are equal (i.e., A=B). While the standing wave wavenumber may not affect the wave amplitude in time or space, Jay (1991) shows that additional funneling effects independent of the wavenumber scale with convergence. Thus, we find that for a given friction $\frac{r}{\omega}$, peak amplification occurs (see also Supporting Information):

$$when\ k \to 0 \quad \eta(x) = \eta_0 e^{0.5xL_a^{-1}}, \#(Equation\ 5)$$

which shows that amplification at *k=0* is also independent of the dynamics associated with incident and reflected waves (i.e., Equation 1). For each wavenumber, peak amplification occurs when k→0, which occurs

$$for\ k_0 \to 0 \quad h \to \infty, \#(Equation\ 6.1)$$

$$for\ k_f \to 0 \quad \underbrace{\frac{r}{\omega}}_{friction} = 1i, \#(Equation\ 6.2)$$

$$for\ k_j \to 0 \quad \underbrace{\Delta}_{convergence} = \sqrt{\underbrace{-1}_{acceleration} + \underbrace{i\frac{r}{\omega}}_{friction}}. \#(Equation\ 6.3)$$

Equations 6 shows that as convergence decreases, the solution for k_j becomes equivalent to k_f, and as friction decreases, Δ becomes *1*. This Δ_C=*1* relationship, like the earlier approximation reached through scaling assumptions, is a balance of convergence and acceleration. Without convergence (i.e., k_f), friction only attenuates tides. However, when convergence is simulated with a reflected wave (e.g., Equation 1) and $\frac{r}{\omega}$>1, k_f nearly captures the same amplitudes as k_j when (see Supporting Information text, Figure S1, and Section 5.3).

When friction and convergence are accounted for analytically (i.e., k_j), peak amplification occurs when convergence is balanced by acceleration and friction in a complex term:

$$\lim_{k_j \to 0} \Delta\left(\frac{r}{\omega}\right) = \Delta_C + i\Delta_+, \#(Equation\ 7.1)$$

where the imaginary component Δ_+ is the convergence at which maximum wave amplification occurs,

$$\Delta_+ = Im\sqrt{-1 + i\frac{r}{\omega}}, \#(Equation\ 7.2)$$

and the real component Δ_C is critical convergence,

$$\Delta_C = Re\sqrt{-1 + i\frac{r}{\omega}}. \#(Equation\ 7.3)$$

Equation 7 is further tested and discussed in Sections 5 and 6 and more explicitly derived in the Supporting Information.

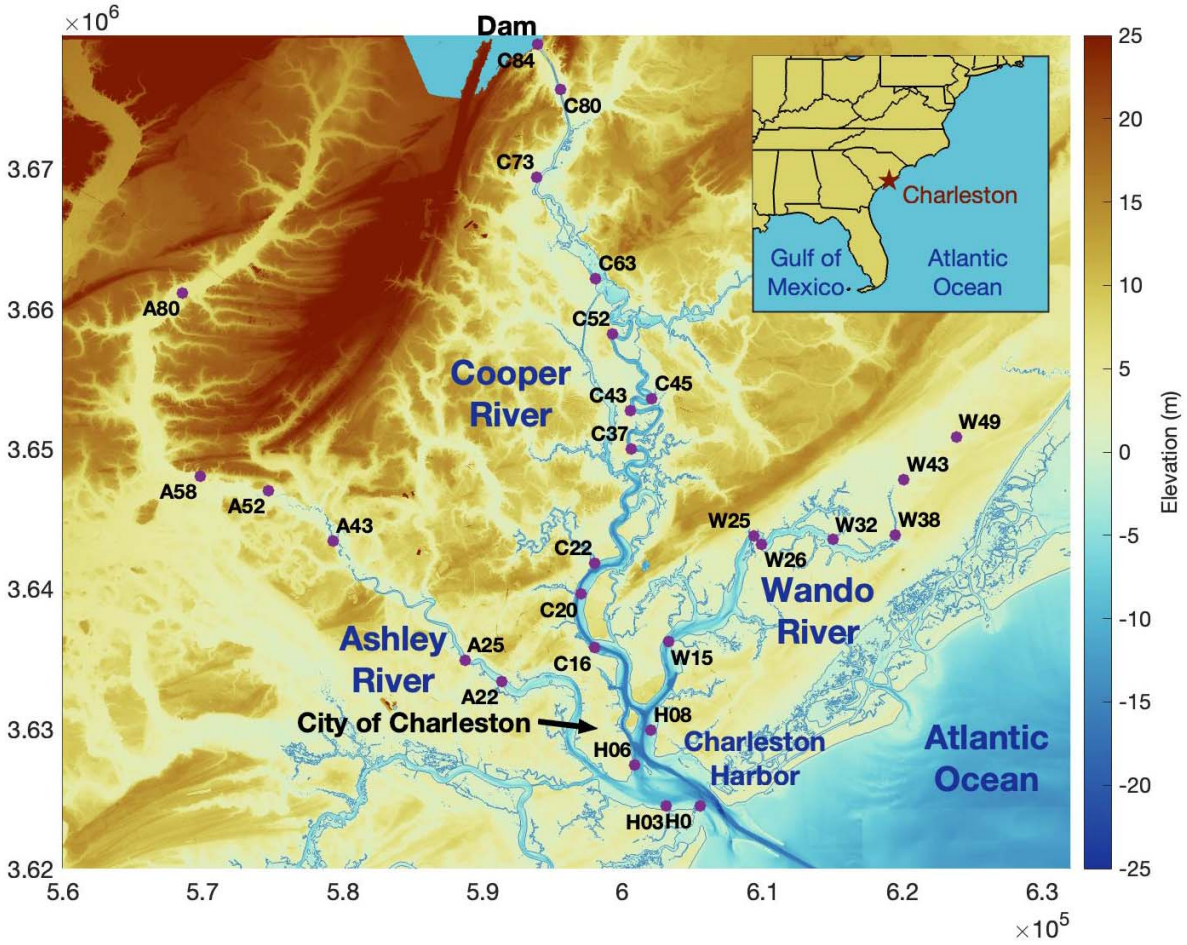

Figure 1. Map of the greater Charleston Harbor System, highlighting the location of water level stations (purple dots).

3 Study Site: Charleston Harbor Rivers

The Ashley, Cooper, and Wando rivers flow into Charleston Harbor, a partially mixed estuary on the South Atlantic Bight (Figure 1). The city of Charleston lies at the confluence of the Ashley and Cooper Rivers. Since the mid 20th century, flood frequency in Charleston

increased from 2 to 25 events per year and—due to sea level rise—is predicted to more than double in the next half century (Morris & Renken, 2020; Sweet & Park, 2017). Despite large scale dredging and harbor modifications (U.S. Department of Commerce, 1989), observations of mean tidal range (1.6 m) in the Charleston Harbor show only minor changes since the 1850s (Talke & Jay, 2020).

The Charleston Harbor watershed is small, not extending beyond the coastal plain (2,860 km^2), and historically (pre-1942) had a combined mean river discharge of less than 10 m^3s^{-1} (Kjerfve & Magill, 1990). Landward of the harbor, the watershed areas of the Ashley, Cooper, and Wando rivers are respectively equal to 915, 1,550, and 293 km^2, and their main channels have relatively similar lengths (~90, 80, and 50 km, respectively). Each river is shallow and convergent in depth, width, and area (Figure 1, see cross-section DEM Figure S4). Historical maps suggest that, prior to the 19th century, river channels had similar geometries and extensive Tupelo-Cypress swamp headwaters (e.g., Faden et al., 1780).

A river to the north of the Charleston watershed, the Santee River, continues to influence freshwater flows and sediment transport in the harbor, due to human interventions. An early 19th century canal connecting the Santee River to Charleston through the Cooper River swamp was replaced with a larger channel that diverted most of the Santee River flow down the Cooper River through a series of dams, starting in 1942. The Santee River diversion resulted in rapid siltation of the Charleston Harbor and—in 1985—most of the river flow was diverted back to the Santee River via Lake Moultrie Reservoir (Althausen & Kjerfve, 1992; Kjerfve & Magill, 1990), with a consequent decreased of Cooper River discharge (for further details, see U.S. Department of Commerce, 1989). The post rediversion 1985–2022 mean discharge of 144m^3s^{-1} is meant to stabilize saltwater intrusion and has very limited variability (beyond daily water releases, called *power peaking*; e.g., Jay et al., 2016). The Ashley and Wando river discharges remain small. We focus here on the 1985–2022 period.

3.1 Data Sources

Twenty-Five water level records spanning from between 1 and 104 years of length are available from the United States Geological Survey (USGS), the National Oceanic and Atmospheric Administration (NOAA), and the National Estuary Research Reserve, and were used in this study (Figure 1, Table S1). Previously unpublished records were obtained and are

now publicly available (Dykstra et al., 2022b). To supplement spatial gaps between water level stations, we also installed seven additional stations in 2021 using HOBO data loggers (Dykstra et al. 2022b, 2022c). In total, 32 stations are used in this study and are labeled with the first letter representing the body of water (i.e., H: harbor, A: Ashley River, C: Cooper River, W: Wando River) followed by the along channel distance inland from the estuary mouth in kilometers (for example, H0 is Fort Sumpter at the harbor mouth). Nearby non-coincident stations within 500m of each other were assigned the same name (e.g., H0). The longest record, at Charleston Harbor Customs House (H06), has a backup gauge, which we used to supplement gaps and identify them as one station.

All water levels were referenced to the North American Vertical Datum of 1988 and were subsampled to a common hourly interval. Additional discharge data were accessed from USGS 02172002 (station C80). While some data do not temporally overlap, all measurements were concurrent to site H06. Analysis was limited to the rediversion period when changes in river discharge and bathymetry were relatively small (Army Corp of Engineers, 2015). Specific details on data sources, access, and length of records at each station is in the supplemental material (Table S1).

Local ground surface and bathymetric elevations were taken from a merged digital elevation model (DEM; CIRES, 2014). Poor data were removed (e.g., water surface elevations in inland reaches). The 3m resolution Cartesian coordinate DEM was subsampled to analyze the geometry of each river along the longitudinal axis. Following the centerline, at 10m intervals, perpendicular cross-sections (2m width resolution) were interpolated to create a longitudinal DEM (Figure S4; Szot & Dykstra, 2022). To calculate the channel geometry of each cross section (e.g., area, width, and mean depth), the water surface elevation of Low Lower Water was approximated at each station (3.5 percentile based on 1/24.8) and linearly interpolated.

4 Methods

4.1 Timeseries Analysis

Observed water levels were decomposed into subtidal and tidal components using a Lanczos filter with a cutoff period equal to 1.7 times the window size (e.g., Dzwonkowski et al., 2015). For the tidal signal, a sensitivity test revealed that the least spectral leaking occurred with window sizes of 35 hours and >45 hours. For subtidal water levels, the magnitude of setup-

setdown was similar to the ~24 cm intraannual variability of the South Atlantic Bight (Parker, 2007). To differentiate setup-setdown from intraannual variability, a 35-hour–2-month band-pass was utilized, a process that also removed sea level rise, which is required to make data stationary (Ghanbari et al., 2019). Extreme setup-setdowns are caused by storm surge events and, using extreme value analysis (e.g., Generalized Pareto Distribution, GPD), the frequency distribution of the tail has a distinct shape which is differentiated from non-extreme events by a threshold (Ghanbari et al., 2019). Setup-setdown heights were fit to a GPD using a peak-over-threshold method (i.e., partial duration series) composed from the 104-year record at H06. The minimum event threshold is identified by gradually increasing the threshold value (starting from the median) until the shape and scale parameters converge (e.g., Ralston et al., 2019), and was found to be 43cm (Figure S5). A total of 32 events were above this threshold, with 14 occurring post rediversion.

The observations at H06 were used to evaluate the propagation of surge and its magnitude transformation along each of the rivers. For setup-setdown, the lag time *tx* at each station to the Charleston Custom House was determined by using cross-correlation with H06 and finding the temporal offset with the highest correlation. Offsetting the data to the highest correlation, the relative magnitude was found using the slope of a line fitted to all available data of each subtidal water level relative to H06:

$$\eta(relative\ magnitude) = \frac{\eta(x, t + tx)}{\eta(H06, t)} \#(Equation\ 8)$$

Tidal harmonic analysis (Pawlowicz et al., 2002) was used to evaluate amplitude variability and phase progression in each river and investigate reflection effects. To minimize the effects of various lengths of record, only the periods of highest spatial coverage and consistent power peaking were used. This includes 30 days in 2021 (May 26–June 1, June 4–14, and August 4–18). Only constituents with signal to noise ratios >2 were retained (Pawlowicz et al., 2002). Tidal reflection at the Cooper River dam was quantified by separating incident and reflected wave trains for M2 and M2 overtides at C73, C80, and C84, covering an 11-km region (Díez-Minguito et al., 2012).

4.2 Mathematical Modeling

For a more general investigation of reflected wave dynamics, observational results were compared to theory using a 1-dimentional semi-analytical tide model developed by Talke et al.

(2021), based on Dronkers (1964). The model was chosen because the solution—Equation 1—identifies contributions from reflected and incident waves. The piecewise consistent channel model solves the shallow water wave equation (Equation 1) after linearizing friction (Equation 3) and in the frictional wavenumber k_f (Equation 4.2). A single sinusoidal wave is prescribed at the open boundary, and a reflective (no flow) boundary condition is applied at the head. Similar to a 1D numerical model, the model is divided into multiple segments, each with a prescribed width, depth, and drag coefficient, allowing us to control the overall geometry and funneling rate. For each segment, Equation 1 is solved iteratively, using a matrix inversion, until the two unknowns, A and B, change by less than 0.1% between successive approximations. Model cross sections are rectangular and assumes all flow is in the channel, river velocity $U_r<U_t$, and $\eta \ll h$. Alternative approaches using numerical models (e.g., Ralston et al. 2018; Figueroa et al., 2022) and many exponential analytical models (e.g., Friedrichs & Aubrey, 1994; van Rijn, 2011) cannot explicitly separate incident and reflected waves (but see Jay, 1991 in the Supporting Information).

We develop four idealized model geometries which approximate the Cooper River using 1km segments (Figure 2). First, a non-convergent geometry had consistent widths and heights, representing the shipping channel. Second, for a more realistic convergent geometry, the width and height decreased in the upstream direction according to the observed e-folding lengths (L_w and L_h, respectively, see Section 5.1). These initial models have lengths of 300 km, representing infinitely long channels, and were shortened to 84 km, representing the dammed Cooper River with two more channel geometries.

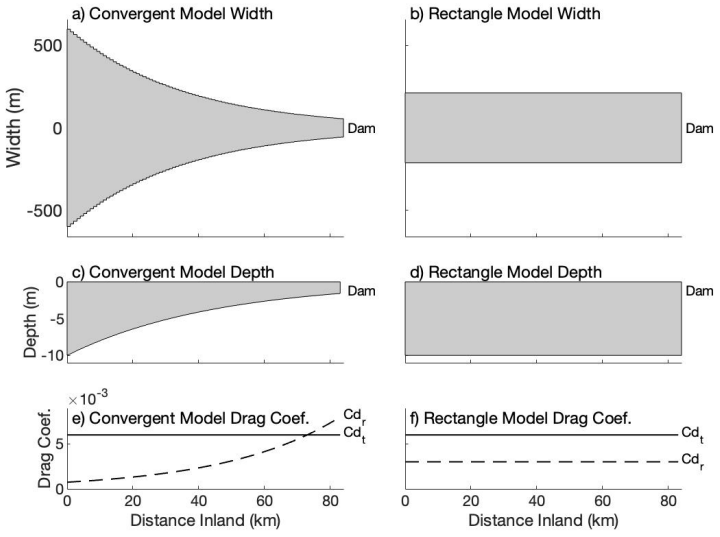

Figure 2. Model setup of a,b) width, c,d) depth, and e,f) drag coefficients for the a,c,e) idealized convergent Cooper River and b,d,f) a comparable rectangular channel.

Adjustments to the model were made to account for friction caused by river flow by applying the following approximation of the drag coefficient:

$$C_d(x) = C_{dw} + C_{dr\infty}\frac{\left[{}^{Q_r}/_{a_\infty}\right]^2}{\left[{}^{Q_r}/_{a(x)}\right]^2} \#(Equation\ 9)$$

where C_{dw} is the long wave drag coefficient, $C_{dr\infty}$ is the river drag coefficient inland of tides, and a_∞ is the area inland of tides. The second term in Equation 9 causes the river contribution to friction to scale inversely with area, as commonly done in tidal environments (Buschman et al., 2009, Kästner et al., 2019), but does not directly model river inflow.

The model is used to explore both tidal dynamics and evaluate the physics of other long waves—such as storm surge. The Cooper River Model closely replicates M2 wave observations across the harbor and Cooper River with a RMSE of 0.039m, suggesting good model validation (see full results presented in Section 5.3). Further validation of the model at higher frequencies is presented in the Supplemental Materials using M2 overtides (Figure S6). Long-wave surge dynamics are explored by approximating the amplitude and primary wave period of observed events. A similar approach was used by Famikhalili et al. (2020, 2022), supported by observations demonstrating estuarine long waves in the weather frequency band have waveforms like tides (e.g., Proudman, 1955; Schumann & Brink, 2009; Yankovsky & Iyer, 2015). While useful for describing and understanding wave dynamics, our analytical approach is idealized and may be inappropriate for assessing flood risk or management strategies.

The validated model was then utilized to study tidal dynamics across the friction and convergence ranges of commonly observed estuaries (i.e., $\frac{r}{\omega}$~0.3–10, Δ~0–3; Talke & Jay, 2020). Friction was simplified with no river effects (C_d=C_{dw}) or height changes, representing funneling in only the width. To capture the range of $\frac{r}{\omega}$ and Δ, we made systematic changes in C_d (0.002–0.0063) and L_w (8–160km), respectively, while other variables were consistent (h:5m, η_0:1m, U_t at mouth:1ms^{-1}, and ω:M2 frequency). These results are presented in the friction-convergence parameter space.

5 Results

5.1 Convergent River Geometry

We first examine landward funneling effects on tidal amplitudes for an idealized, exponentially converging model using the non-dimensional friction-convergence parameter space. Modeled results are then compared to real estuaries. Figure 3a shows the relative

amplitude ($\frac{\eta(L_a)}{\eta_0}$, i.e., at x=L_a, normalized by the mouth amplitude x=0) changes with friction and convergence. The isoline of 1—showing no amplitude change—has a convergence that ranges an order of magnitude within the parameter space (Δ~0.2-2) and is in near agreement with the analytically defined critical convergence Δ_C. The maximum relative amplitude Δ_+ also matches the model and has a similar trend. Both Δ_C and Δ_+ increase with friction, a result of modeling friction with a complex wavenumber (i.e., k_f, k_j, Equation 4), in contrast to assumptions based on simplifying the wavenumber to only real terms, e.g., Δ_C=1, (Talke & Jay, 2020; further shown in Figure S2), which produces the same Δ_C as if there was no friction at all (i.e., k_0, Equation 6.1). For a given friction, a higher convergence (a shift up in Figure 3) only increases amplitudes to Δ_+, above which amplification is less. At extreme convergences (large Δ), amplification becomes negligible. For a conceptual example, tidal waves amplify in long funneling estuaries and not short coastal bays.

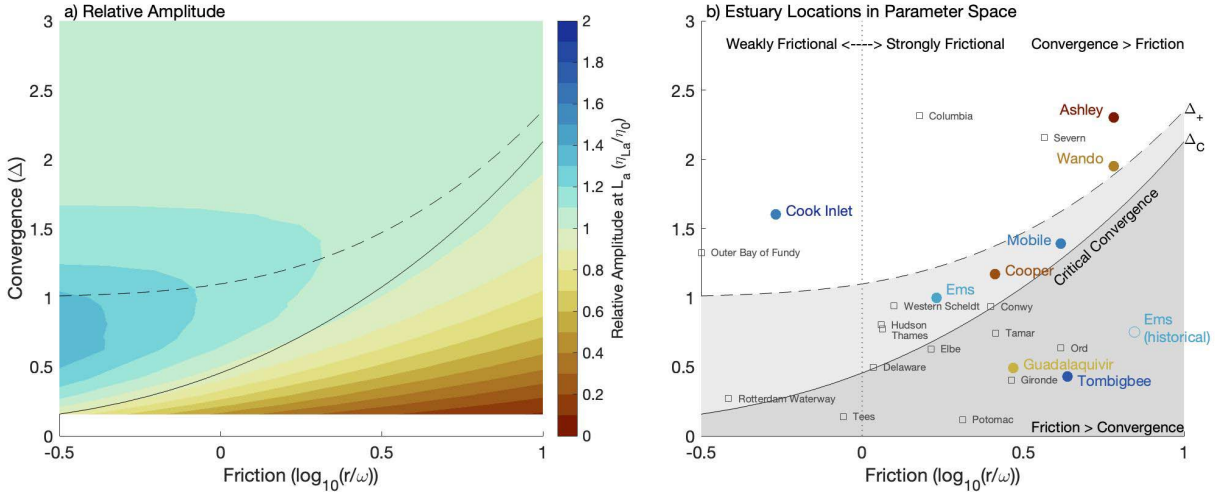

Figure 3. Nondimensional friction-convergence parameter space, showing a) tidal amplification and b) the relative location of 23 estuaries. a) Amplification is calculated as the tidal amplitude at one e-folding length (L_a) relative to the mouth. The parameter space is delineated by dissipation into weakly and strongly frictional regimes (r=ω, vertical dotted line) and at critical convergence (Δ_C; solid line). Amplitude is constant at Δ_C and amplifies above or attenuates below the Δ_C line. For a given friction, maximum amplification is reached at Δ_+ (dashed line). Data sources were various: Ashley, Cooper, Wando (this study); Mobile and Tombigbee (Dykstra et al., 2022); Guadalaquivir (Díez-Minguito et al., 2012); Ems (Talke & Jay, 2020); Cook Inlet (Danielson et al., 2016); gray squares (Lanzoni & Seminara, 1998, updated by Toffolon et al., 2006). The parameter space represents the ranges of $r = \frac{8}{3\pi}\frac{C_d U_t}{h}$ and $\Delta = \frac{1}{4\pi}\frac{\lambda}{L_a}$ commonly observed in estuaries (Talke & Jay, 2020).

We next determine where Ashley, Cooper, and Wando rivers lie within the friction-convergence parameter space of Figure 3, based on tidal conditions and geometry. Each river branches from Charleston Harbor at a similar distance inland and each has similar tidal conditions at the mouth (river kilometer rkm ~7–9; Figure 1). As they branch, the river mainstem channels have similar widths, mean depths, thalweg depths, and cross-sectional areas (Figure 3, S4; note: side-channels, wetlands and tribulates are not captured). Each of these parameters exponentially decay landward at nearly constant rates and are approximated with constant e-folding lengths (Figure 4, Table S2). Overall area funneling $1/L_a$ of the Ashley and Wando are nearly identical (~1/9 km^{-1}) and more than twice the Cooper (1/25 km^{-1}; Figure 4a). While estuarine funneling is traditionally observed and parameterized using width convergence only, assuming a flat bed (e.g., Friedrichs & Aubrey, 1994; Prandle & Rahman, 1980; Winterwerp et al., 2013), here, depth convergence also contributes to area convergence (Figure 4b), and in the Wando, depth convergence exceeds width convergence (Table S2), suggesting that frictional effects may increase landward.

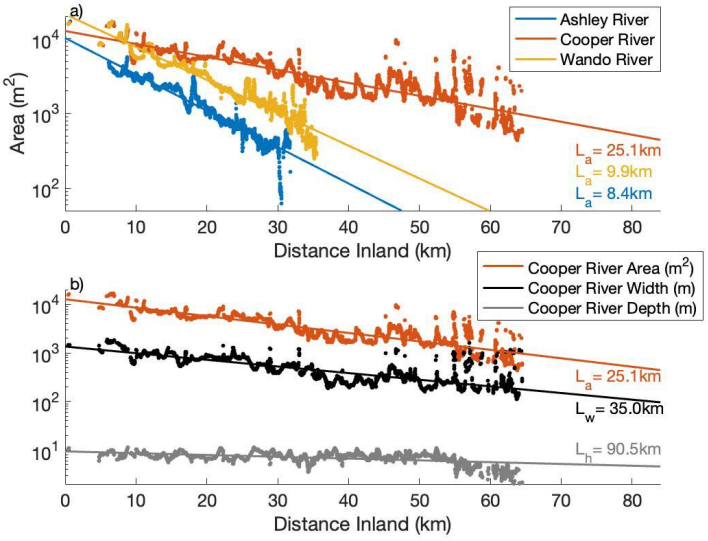

Figure 4. Geometry of the Charleston Harbor subestuaries, shown longitudinally for a) the area of all subestuaries and b) the area, width, and depth of the Cooper River. Observations are shown at 10m intervals (dots) and fit with a line to show the e-folding lengths (slope).

The parameter space location of the Ashley, Cooper, and Wando rivers are presented with 21 other estuaries (Figure 3b). Most estuaries are strongly dissipative (r>ω, i.e., $\log_{10}\frac{r}{\omega}>0$) and many are near critical convergence (e.g., $\Delta_C \doteq \Delta/4$), such as the Cooper River, Mobile Bay, and Ems Estuary. Relative to the Cooper River, the Ashely and Wando Rivers are more convergent and more dissipative (up and to the right in Figure 3b). Even though the Ashley River is more convergent, the Wando River is closer to Δ_+, suggesting the Wando River amplification is larger. Delineating frictional regimes in reference to dissipation alone is inadequate (i.e., dotted line at

448 $\log_{10}\frac{r}{\omega}$=0). Here, critical convergence delineates the lower *weakly convergent regime* ($\Delta<\Delta_C$),
449 where funneling effects are weaker than friction, from the upper *strongly convergent regime* (Δ_C
450 $<\Delta<\Delta_+$), where funneling effects are stronger than friction. Our regimes delineate the
451 descriptions of Lanzoni & Seminara (1998). As funneling becomes strong enough to reduce the
452 maximum amplification, a further distinction is required, which we call the *hyper-convergent*
453 *regime* ($\Delta>\Delta_+$). Next, we compare theory to tidal observations and to longer period storm surge
454 waves.
455

456 **5.2 Estuarine Long Wave Observations**

457 *5.2.1 Description of a Storm Surge Event*

458 Atlantic Ocean water levels at Charleston Harbor oscillate with tides and weather
459 patterns, generating waves that propagate landward. Results show that, at the weather frequency
460 band, setup-setdown commonly exhibits longer periods (~4–10 days) and smaller amplitudes
461 (~10–20 cm) than the semidiurnal tide, factors that make the waveform be more convergent and
462 have lower friction, respectively (Equations 2 and 3). In parameter space, relative to the tide,
463 setup-setdown would be up-left in the hyper-convergent regime of Figure 3. The largest setups
464 are storm surges. We next describe the dynamics of the third largest (positive) storm surge event
465 in the Cooper River since re-diversion: a 2009 December winter storm (Figure 5; we do not
466 consider the two larger events because they are marked by sizeable negative surges and power
467 peaking anomalies).

468 Water levels measured during the December 2009 event (Figure 5a) clearly consist of
469 semidiurnal (approximately tidal) fluctuations (Figure 5b) and a longer period storm surge
470 (Figure 5c). In Charleston, the storm surge peaked at 54 cm, with an annual exceedance
471 probability of ~0.12 (~8 year event; Figure S4). Daily peak discharge remained approximately
472 the same during the storm (Figure 5d). Observed water levels show that tides are strongly
473 semidiurnal and became smaller through time, capturing a transition to the smallest tidal
474 amplitudes of the month (monthly beat from M2–N2–S2 harmonics; Figure 5a, b). Tidal low
475 water elevations become higher in the landward direction (Figure 5a), corresponding to a
476 decrease in tidal range and an increase in mean water level. The tidal signal was also delayed,
477 more at low water than high water, suggesting asymmetry and overtide generation.

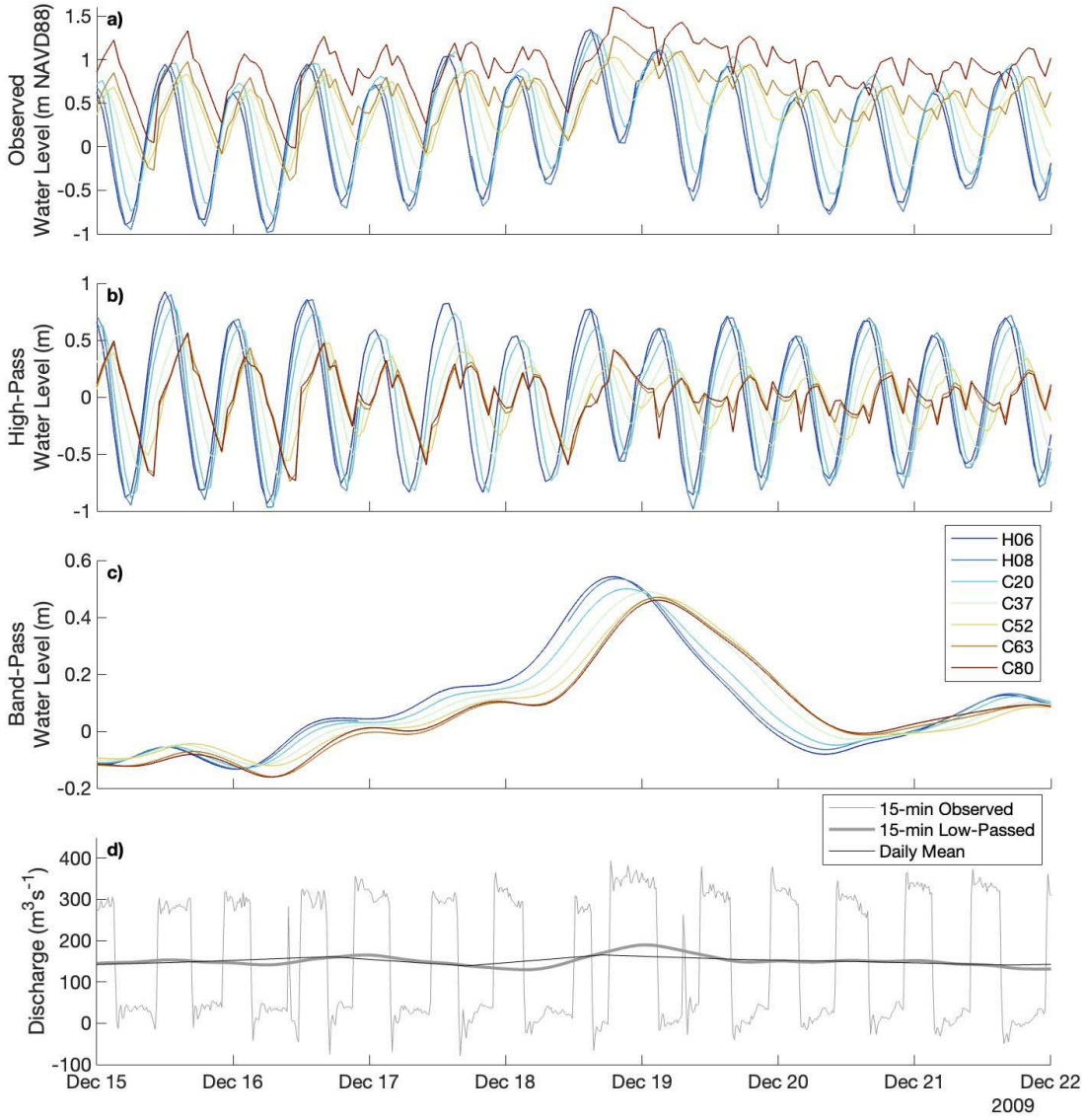

478
479 **Figure 5.** Time series of a storm surge event in the Charleston Harbor and Cooper River,
480 showing 7 days of a) observed water levels decomposed into b) high-passed water levels (35-
481 hour window) and c) band-passed water levels (35-hour–2-month windows) and d) discharge at
482 C80. The decomposition separates the b) tides from the c) storm surge. c) At each station, in a
483 landward direction, the peak contribution from storm surge occurred at a later time, capturing the
484 propagation of a storm surge wave. d) During this time, near the dam, negative discharge
485 captures flooding tides, which are largely overpowered by diurnal dam releases (i.e., power
486 peaking). The small variability of the 35-hour low passed discharge suggests power peaking
487 effects are also filtered in the band-passed water levels (c).
488

The propagation of storm surge followed a similar pattern to the tidal waves (Figure 5). As the winter storm approached, Charleston subtidal water levels at H06 slowly increased 39 cm in 2 days (December 16–18). Subtidal water levels then rapidly increased 38 cm to a peak on December 18 (19:00 GMT; Figure 5c). In the landward direction, stations peaked one after another like the tide (Figure 5c). Approaching the dam (C84), the peak was delayed 8 hours and was near simultaneous at the 3 closest stations (C63, C80, and C84), suggesting the wave stopped progressing, had an infinite phase speed, and was reflected by the dam. Dam subtidal water elevations (C84) raised 37 cm in the last 22 hours, indicating that unlike the tidal wave, the surge wave exhibited almost no attenuation. The region escaped flooding because the surge occurred after high tide and coastal sea-level was near its seasonal low.

5.2.2 Long Wave Dynamics

We next quantify the longitudinal variability of tidal, setup-setdown, and storm surge waves for the Ashley, Cooper, and Wando rivers, using water level data from the period of best spatial coverage (2021). For this period, the amplitude of the largest tidal harmonic (M2) was 0.74 m at the mouth (H0), and then amplified landward across the harbor and all three rivers (Figure 6a). Amplitudes peaked further seaward in the Cooper River (rkm 22) than in the more convergent Ashley and Wando Rivers (rkm 38). Observed amplification was greatest on the Wando, reflecting its parameter space proximity to Δ_+ (Figure 3b). The overtides M4 and M6 exhibit greater amplification than M2, likely due to generation by shallow water frictional interaction (Figure 6c,e). Interestingly, the M2, M4, and M6 peak amplitudes were nearly co-located in the Wando, but, in the Cooper, moved further landward for higher frequency waves. All the tidal harmonics decayed from peak to zero in a ~10–15 km reach along the Ashley and Wando (A43–58 and W38–W49, respectively, Figure 3), but, on the Cooper River, they decayed more gradually and stopped decaying around rkm 60. Landward of rkm 60 tidal waves amplified, suggesting dam induced amplification. Harmonics with higher frequencies amplified more (Figure 6), a relationship quantified in the Supporting Information with the M2, M4, M6, and M8 wave trains showing a near linear wave frequency-amplification relationship (η_r/η_i=2,100ω+0.08, Figure S7).

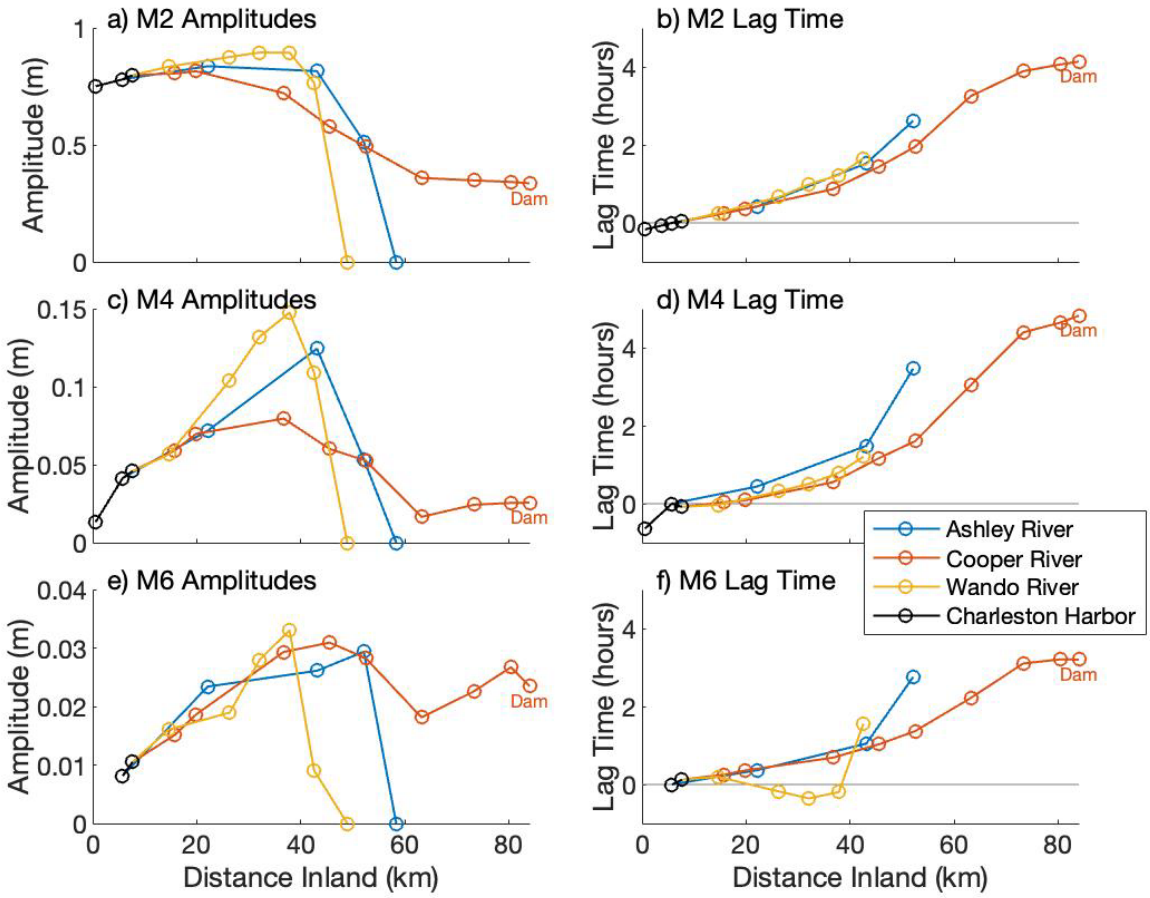

Figure 6. Observed tidal wave amplitudes (left) and lag times relative to H06 (right) for a,b) the principle tidal harmonic, M2, and M2 ovetides, c,d) M4 and e,f) M6. For y-axes, amplitude subplots ranges are variable (a,c,e), while phase subplot ranges are all 360 degrees (b,d,f) and exceed 360 degrees to show relative phase changes with unwrapped phases.

The timing of tides relative to H06 show a general landward delay (Figure 6b,d,f). In each river, the lag times of M2, M4, and M6 were similar, as expected, because they are created by M2 (Godin, 1999). Lag times in the Ashley increased landward exponentially, indicating a slowing wave celerity, likely due to shallowing. The Cooper had somewhat shorter lag times (e.g., rkm 40–50), indicating faster wave celerity, with the line flattening as the as the waves approach the dam, showing very little or no time lag like a standing wave. For higher frequencies, the lag-time flattening occurred closer to the reflection point (Figure 6b,d,f). The Wando M6 lag time decreased landward, perhaps indicating that the mechanism generating the overtide was changing (Gallo & Vinzon, 2005), possibly because of the strong depth convergence on the Wando.

An examination of longitudinal subtidal variability from coastal setup-setdown suggests that longer period waves attenuate less and have longer lag times than tidal waves (Figure 7a,b). On the three rivers, all observed setup-setdown magnitudes from 2021 were within 12% of H06, indicating small longitudinal variability (Figure 7a). For the lag times, setup-setdown was delayed in a landward direction, similar to tides, demonstrating these signals also propagate as long waves (Figure 7b). Unlike the tides, setup-setdown lag times were much larger, indicating the longer period wave celerity was slower.

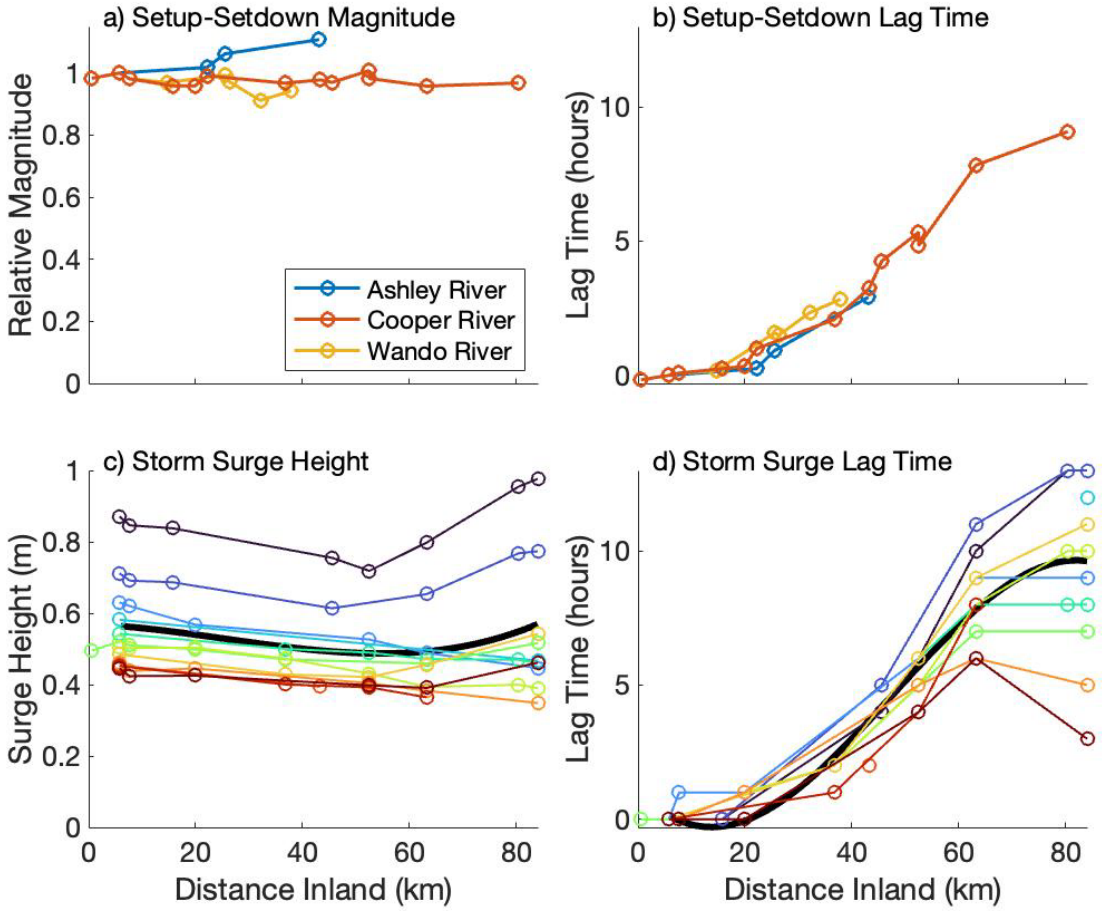

Figure 7. Observed low frequency wave a,c) magnitudes and b,d) lag times for a,b) all 2021 setup-setdown and c,d) 12 individual storm surge events on the Cooper River (post 1985). For a and b, only stations with high coorelation are shown (R>0.9). For c and d, connecting lines are shown for events with more than 3 station observations and, for all observations, a cubic fit is shown (black line).

The 2021 setup-setdown composite had amplitudes and lag time progressions similar to the largest individual setup-setdown events at H06, which we classified as storm surge waves (setup-setdown heights>43cm, maximum=88cm; see methods). Two events were not included

552 due to large changes in the power peaking schedule modulating water levels at subtidal
553 frequencies. To the mid estuary, surge heights decreased by ~10% and lagged by 4–5 hours
554 (Figure 7c,d), like the 2021 setup-setdown waves (Figure 7a,b). Further landward, of the 10
555 events observed at the dam (C79 or C83), 7 events amplified in the upper estuary and, in 5 cases,
556 surge heights at the dam exceeded heights observed in Charleston (H06). Lag times also stopped
557 increasing as they approached the dam (Figure 7d), with peak surge water levels occurring
558 almost simultaneously, similar to the tidal observations (Figure 5b,d,f). Contrasting the events
559 by storm surge height (ascending red to blue) reveals the largest events were delayed twice as
560 long (Figure 7d) and amplified more approaching the dam (Figure 7c). We implicitly assume
561 that local wind forcing is a negligible factor in the evolution of water levels, given the similar
562 evolution of different events and the relatively small fetch the sinuous channels provide wind,
563 even when blowing in the right general direction (e.g., Jay et al., 2015).
564

565 **5.3 Modeled Incident and Reflected Waves**

566 We next use analytical model results to investigate the influence of convergence and both
567 partial and full reflections on the evolution of both semidiurnal tidal amplitudes (left column,
568 Figure 8a,c,d) and longer period waves (2 day period; right column, Figure 8b,d,e). For a
569 geometry based on the Cooper River (Figure 2), the influence of convergence is elucidated by
570 comparing waves and phases obtained using constant width (red lines) and convergent (blue
571 lines) geometries (Figure 8); similarly, the influence of the dam on the incident and reflected
572 wave is obtained by running the model with and without a reflective boundary (blue and yellow
573 lines, respectively). For each scenario, the incident (solid line) and reflected (dashed line) wave
574 amplitudes are also shown (Figure 8c,d,e,f). We test model scenarios using sinusoidal
575 waveforms with the same boundary amplitude (0.74m) and two different periods, representing
576 the M2 tide and a 2-day storm surge, a midrange period of commonly observed storm surge
577 waves (Familkhalili et al., 2020).

578 Model results for the Cooper River geometry suggest that convergence strongly
579 influences the spatial variation of amplitude at the semidiurnal frequency (Figure 8a), but
580 produces only small differences between scenarios at the surge (2 day) frequency (Figure 8b).
581 Model results well reproduce measured M2 behavior (RMSE: 0.039m; Figure 8a) and
582 qualitatively resemble many of the observed storm surges (Figure 7c). Inspection shows that the

583 incident and reflected waves are substantially influenced by the wave frequency, which enters
584 both the Δ and $\frac{r}{\omega}$ parameters (Equation 2 & 3), which contributes to wave phase, controlling the
585 total wave amplitude (i.e., kx-ωt, Equation 1).

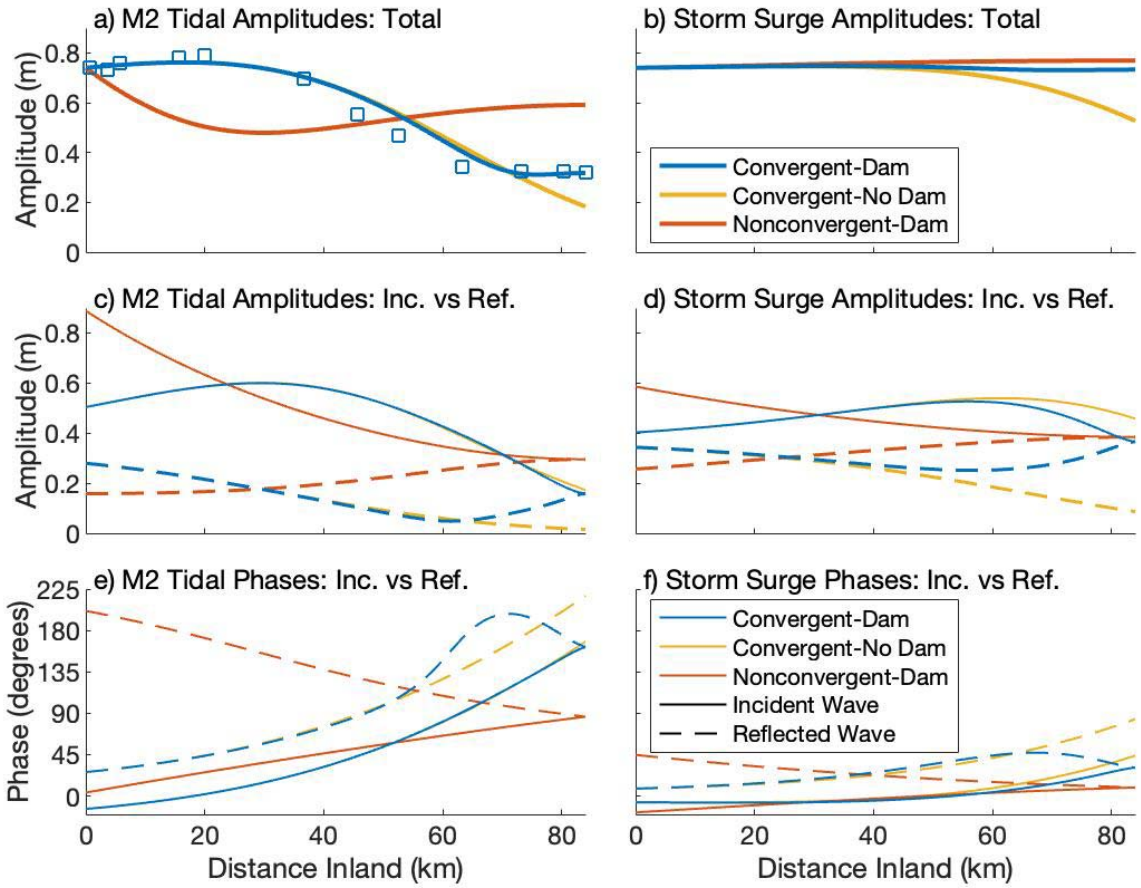

586
587 **Figure 8.** Modeled M2 tidal waves (left) and 2-day storm surge waves (right) using Equation 4
588 and simplified geometries based on the Cooper River. Total combined wave amplitudes (a,b;
589 thick lines) are decomposed into incident and reflected wave amplitudes (c,d; narrow lines) and
590 phases (e,f; narrow lines). Colors show different modeled geometries for the convergent Cooper
591 River with and without a dam (blue and yellow, respectively) and a nonconvergent rectangular
592 channel (red; see Figure 2). For subplots c–f, linetypes show the incident (solid) and reflected
593 waves (dashed). a) The M2 tidal wave model closely matches observations (blue squares;
594 RMSE: 0.039m). In some regions the model senarios were same and are masked by the blue
595 lines. The nonconvergent-no dam scenario had a total wave that was nearly identical to the
596 incident wave of the nonconvergent-dam scenario (c,e) and is not shown.
597

598 For a channel with constant width and depth, the nonconvergent-dam geometry reveals
599 landward attenuation of the total combined M2 wave across the lower estuary, followed by
600 amplification, reaching almost the same amplitude at the dam as the mouth (red, Figure 8a).

Separating incident and reflected waves shows consistent attenuation and phase increase, first landward to the dam in the incident wave, and then seaward in the reflected wave (Figure 8c,e). Without any reflection, the nonconvergent-no dam scenario has a total wave that was nearly identical to the incident wave (Figure 8c,e) and is not shown.

With convergence, the incident wave amplitude exhibits a maximum at both ~12-hour and ~48 hour frequencies, but in substantially different locations (~35 and 60km from the mouth, respectively). In both cases, reflected wave amplitude exhibits a minimum approximately 20-25 km from the dam (see blue dashed lines in Figure 8c,d), just downstream of the maximum reflected phase (Figure 8e,f). Incident and reflected amplitudes of the 2-day wave, combined with the phases (Figure 8f), leads to the approximately constant wave amplitude observed in Figure 8b; hence, the apparent similarity with the non-convergent channel scenario hides substantial differences in their reflection dynamics. By contrast, incident and reflected waves of the M2 wave lack symmetry, and lead to the observed S-shaped curve in tidal amplitudes and a strong difference with the M2 non-convergent channel scenario (Figure 8a,c,e).

The phase progression for both incident and reflected waves is strongly curved near the dam, and suggests strong spatial gradients in the wave celerity. Moreover, a maximum is formed in the phase progression of the reflected wave near the dam, more prominently at the M2 frequency than at the storm surge frequency (blue dashed line, Figure 8e, f). The maximum phase in the reflected wave leads to the non-intuitive conclusion that the reflected wave reaches the ocean boundary before it starts at the dam (Figure 8e; M2 wave); a similar, upriver phase progression is also observed for the 2 day reflected wave (Figure 8f). This behavior occurs because the phase shift in a partial reflection is non zero and is strongly phase-locked in our configuration to the incident phase. The phase locking occurs due to partial reflection points that are distributed evenly throughout the estuary (see discussion, Section 2, and below); a slight variability in the relative phase of the incoming and outgoing wave occurs, due to variations in velocity and hence friction (see the convergent, no-dam case). The maximum in reflected phase occurs because of the interaction of the total reflection (phase shift of zero degrees, progressive phase variation) and the locally generated partial reflection. Near the dam, substantial differences in amplitude and phase are observed between the case with a dam (blue line) and the no-dam case (yellow line), indicating a region of dam influence (Figure 8c–f). Upstream of the reflected

632 phase maximum, the reflected amplitude and phase progression is nearly a continuation of the
633 phase progression of the incident wave, but in the opposite (seaward) direction. As dam
634 influence subsides in the seaward direction, the phase difference in the reflected wave relaxes to
635 the phase shift caused by partial reflection only (yellow dashed line, Figure 8e,f).
636 Reflection dynamics differ strongly by wave period (Figure 8). Phase and amplitude
637 differences between the dam and no-dam cases persist for a longer distance downstream for the
638 surge wave than the M2 wave, and are more pronounced for the reflected than the incident wave
639 (compare blue and yellow lines in Figure 8c and 8d, or 8e and 8f). Both these observations are
640 influenced by friction; the reflected M2 wave, with a higher velocity (due to both larger
641 amplitude and higher frequency), is attenuated more quickly than the surge wave. The reflected
642 wave influences the net velocity, and therefore the friction is felt by both the incoming and
643 reflected wave. For this reason, the incoming wave is slightly different between the no-dam and
644 dam cases, with a bigger influence observed at the surge frequency, likely because the reflected
645 wave persists longer (yellow vs. blue lines near the dam in Figure 8c vs. Figure 8d).
646
647 The phases observed in the convergent and non-convergent geometries reveal different
648 spatial variations in constructive vs. destructive interference. The nonconvergent-dam geometry
649 reveals landward attenuation of the total combined M2 wave across the lower estuary, followed
650 by amplification, reaching almost the same amplitude at the dam as the mouth (red, Figure 8a).
651 Near the dam, phases of the incident and reflected wave are similar, capturing constructive
652 interference, which caused the amplification. Phase difference became greatest in the lower
653 estuary, causing significant destructive interference.
654 In a convergent estuary, funneling influences the incoming and reflected wave
655 asymmetrically (Jay, 1991), with the reflected wave at the dam attenuating over a shorter
656 distance due to the area divergence. Hence, for the configurations shown here, the transition to
657 destructive interference (greater than 90º phase difference between incident and reflected waves)
658 almost happens for the 12-hour wave—reaching 88º—and is not close for the 2-day wave
659 (reaching 40º; Figure 8e,f). At locations seaward of ~rkm 60, the phase difference between the
660 incident and reflected wave is dominated by partial reflection and is 40º–47º for the M2 wave
661 and 15º–33º for the surge wave. For the convergent-no dam scenario, similar phase differences
662 occur because partial reflection dominates everywhere (yellow, Figure 8e,f). Thus, for our

configuration and scenarios, partial reflection always causes constructive interference. The phase lag is larger for the M2 wave than the surge wave, because phase speed is similar while wave period is less. The larger M2 phase lag reduces constructive interference and, for the regions where the M2 incident wave is not amplifying (i.e., x>~30rkm), causes the total M2 wave to be smaller than the total 2-day surge wave (Figure 8a, b). To summarize the trends of reflected waves, the direction that phases increase and amplitudes decrease are *seaward* for fully reflected waves and *landward* for partially reflected waves—a result of being phase locked to the incident wave (Figure 8c, e). By evaluating only the total wave amplitude (Figure 8a), as traditionally done (e.g., Chernetsky et al., 2010; Ensing et al., 2015; Li et al., 2016), trends suggest dam effects extend seaward for 12 km (rkm 72), but by decomposing the waves, we see dam effects exceed convergence effects for 21 km (rkm 63), almost twice the distance seaward.

For the Cooper River, the model indicates the dam elevates high water levels of 2-day large surge events for the landward half of the river, exceeding 30% near the dam (blue and red lines, Figure 8b). The nonconvergent scenario suggest further channelization of the Cooper River will moderately increase the magnitude and seaward extent of dam effects, potentially increasing the likelihood of flooding in the city of Charleston.

6 Discussion

6.1 Expanding the Friction-Convergence Parameter Space for All Long Waves

Long waves in channels are controlled by channel geometry and wave characteristics. Like many other regions, the Charleston Harbor rivers are marked by multiple types of long waves, with amplitudes and periods as small as the M6 overtide (T≈4 hours), and as large as meteorologically generated storm surge and setup-setdown waves (T≈1–14 days). In the same estuary region, the mechanics of each wave are different, which we discuss for the Cooper River in a friction-convergence (Δ,$\frac{r}{\omega}$) parameter space (Figure 9). We use both measurements and the idealized model to delineate where the typical tides, storm surge, and long-period setup in the Cooper River and Charleston Harbor are in (Δ, $\frac{r}{\omega}$) parameter space (Figure 9). To gain insight into general tendencies, each wave-type is considered independently. Because different waves (e.g., tides and surge) interact nonlinearly (e.g., Parker, 2007, Jay et al., 2016), some variability

between idealized model results (e.g., Figure 8b) and observed waves (e.g., Figure 7c) is expected, however, the enhanced frictional loss and nonlinear interaction usually only modifies—rather than completely changes—the amplitude and phase progression of each wave (Familkhalili et al, 2020; Godin, 1999; Yankovsky & Iyer, 2015). In Figure 9, mean channel geometry and observed wave characteristics (using H0 observations like our boundary conditions) reveal tidal harmonics each at a single point (circles) and meteorological waves with boxes, corresponding to the observed range of periods and amplitudes. For larger amplitudes, waves have higher friction parameter values due to larger velocity amplitudes. For larger periods, waves have larger convergence parameter values—small changes in $\frac{r}{\omega}$ occur because $U_t \propto \omega$.

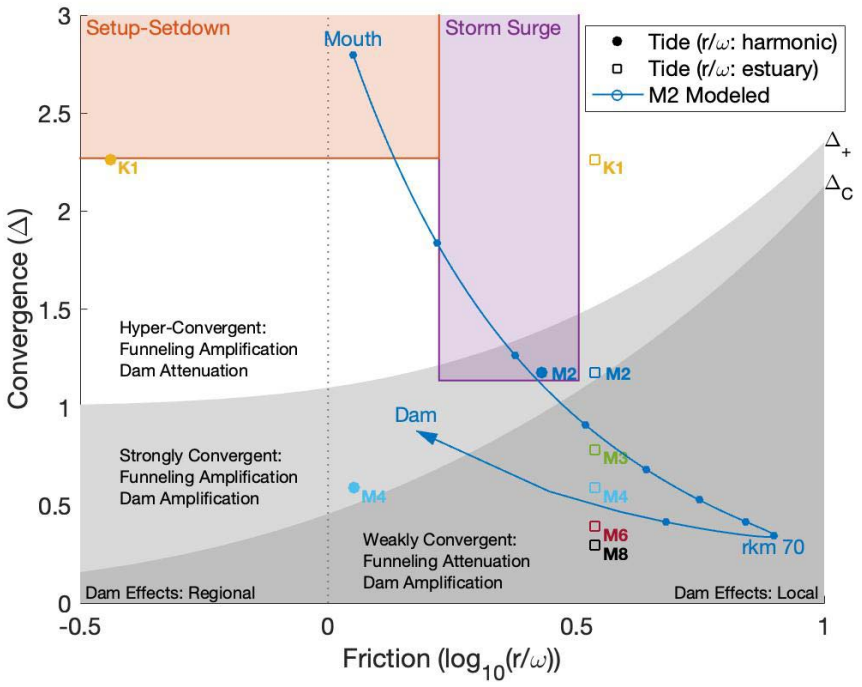

Figure 9. Long waves of Charleston Harbor and their location in friction-convergence parameter space for the Cooper River. Layout follows Figure 3. The parameter space of storm surge and setup-setdown is only partially shown and extends from Δ= 1.1 to 7 and Δ= 2.3 to 16, respectively. Major tidal harmonics are shown with friction estimated from the amplitude (filled circles) observed at H08 and the mean semidiurnal current amplitude (open squares) using a reach-averaged depth, drag coefficient and an approximated velocity scale ($U_t \approx \frac{\eta \omega L_a}{h}$, Friedrichs, 2010). The friction of M3, M6, and M8, are at log10(r/ω)<–0.5. M2 modeled in a convergent geometry with a dam (i.e., Figure 8a) shows the longitudinal variability of M2 (blue line) at 10km intervals (dots). All other parameters were determined using observations except storm surge periods, which are 12–72 hours following (Familkalili et al., 2020)

731 The parameter space encompassed by tide, surge, and setup-setdown waves in the Cooper
732 River—as suggested by idealized model results (Figure 9)—corresponds well with the observed
733 spatial variability in amplitudes (Figures 3a, 6, 7). We consider first the part of the estuary
734 dominated by funneling effects, not reflection. Setup-setdown waves, with relatively small
735 amplitudes and large periods, are found in the hyper-convergent regime of small or negligible
736 amplification (see Figure 3a). Surge waves, with larger amplitudes (and velocities), exhibit more
737 friction. Moreover, because surge wave periods (12–72 hours, following Familkhalili et al.,
738 2020) are often less than most setup-setdown events, the convergence value Δ can be smaller.
739 Hence, storm surge is within a regime marked either by amplification (low end of its Δ range) or
740 a nearly constant amplitude, as with setup-setdown waves (Compare Figure 3a, which shows
741 relative amplification, with the Figure 9 parameter space). Similarly, diurnal tides such as K1
742 are found in the hyper-convergent regime marked by amplification or near parity (circles). The
743 semidiurnal M2 tide is in the strongly convergent regime marked by amplification.
744 As the M2 wave in the Cooper River is transformed in the upstream direction by
745 changing tidal velocity, river flow, depth and width variability, and the total reflection off the
746 dam, both Δ (Equation 2) and $\frac{r}{\omega}$ (Equation 3) shift. Hence, M2 begins at the Cooper River
747 mouth with a large Δ ratio and $\frac{r}{\omega}$=1 (blue line, Figure 9) and, as the wave travels upstream,
748 frictional effects increase due to decreased depth and increased river velocity (both of which
749 increase $\frac{r}{\omega}$). Upstream of rkm 70, in the region of prominent dam reflection effects, $\frac{r}{\omega}$ decreases
750 due to decreased tidal velocity. As the wave moves through parameter space (Figure 9), it
751 crosses critical thresholds: the location of peak M2 amplitude corresponds with Δ_+ (~rkm 20),
752 the peak incident wave amplitude corresponds with Δ_C (~rkm 30), and the minimum total wave
753 amplitude corresponds with peak frictional effects (largest $\frac{r}{\omega}$; ~rkm 70). Upstream of this
754 location, dam reflection effects become more prominent (i.e., amplitude of fully reflected wave
755 exceeds the partially reflected wave), causing the wave to shift up-left in parameter space and
756 approach Δ_+, emulating the observed amplification (Figure 6a).
757 Peak amplification from landward funneling at Δ_+—which delineates our hyper-
758 convergent regime—occurs where acceleration is balanced by the forces of convergence and
759 friction (i.e., $\Delta \geq \Delta_+$). From our results, we see M2 amplified more from convergence and
760 exhibited faster wave celerity than storm surge and setup-setdown (Figures 6, 7), providing

observational support that wave proximity in parameter space to Δ_+ increases amplification and celerity. Within the hyper-convergent regime, amplification and celerity are inversely related to wave period and wavelength, becoming minimally affected by convergence and friction as $\Delta >> \Delta_+$. Under these extreme convergences, incident and reflected waves have nearly the same magnitude (i.e., A~B) and low spatial variability. This indicates that storm surge events of relatively short duration amplify and accelerate more than long duration events. Frictional effects are minimal, though, and additional friction from interaction with tides and river discharge adds temporal variability that may shift events horizontally in parameter space; complexities that partially explain the range of observed Cooper River storm surge dynamics (Figure 7c, d).

Amplification of the dominant M2 tides in the more convergent Ashley and Wando rivers was similar to the Cooper River because they were also shallower and had higher friction, placing all of their waves further up and to the right in parameter space—retaining a similar distance from Δ_+ (Figure 3b). For estuaries with much weaker funneling, like the Guadalquivir, Gironde, or Potomac Rivers ($L_w \approx 60$, 87, and 230 km, respectively; Figure 3b), the parameter space of storm surge events would likely extend to both sides of Δ_+, suggesting medium duration events may amplify the most from funneling geometry and the most intense short duration-large amplitude events could attenuate landward the most.

6.2 Effects of Dams in Friction-Convergence Parameter Space

Placing a dam in an estuary affects waves differently depending on where they lie in the $(\frac{r}{\omega}, \Delta)$ parameter space regime, specifically the wave magnitude and how far reflection effects propagate seaward (Figure 10). Using the model configurations of Figure 3a (i.e., constant depth , $L_a=L_w$, and no river flow), a reflective boundary is introduced ($x_{dam}=3L_a$, scales with area funneling L_a to limit the effects of resonance). Figure 10a shows the maximum amplitude change caused by shortening an estuary with a dam in terms of $d\eta_d=(\eta_{dam}-\eta)/\eta$, where η_{dam} is the amplitude of the short estuary. Dam induced amplification increases as convergence decreases (small Δ). Amplitudes are mildly reduced in the hyper-convergent regime ($\Delta>\Delta_+$) and are substantially increased in the strongly and weakly convergent regimes, amplifying waves by >50% for $\Delta<0.5$. A weak dependence on $\frac{r}{\omega}$ is observed, with slightly more amplification in more frictional configurations.

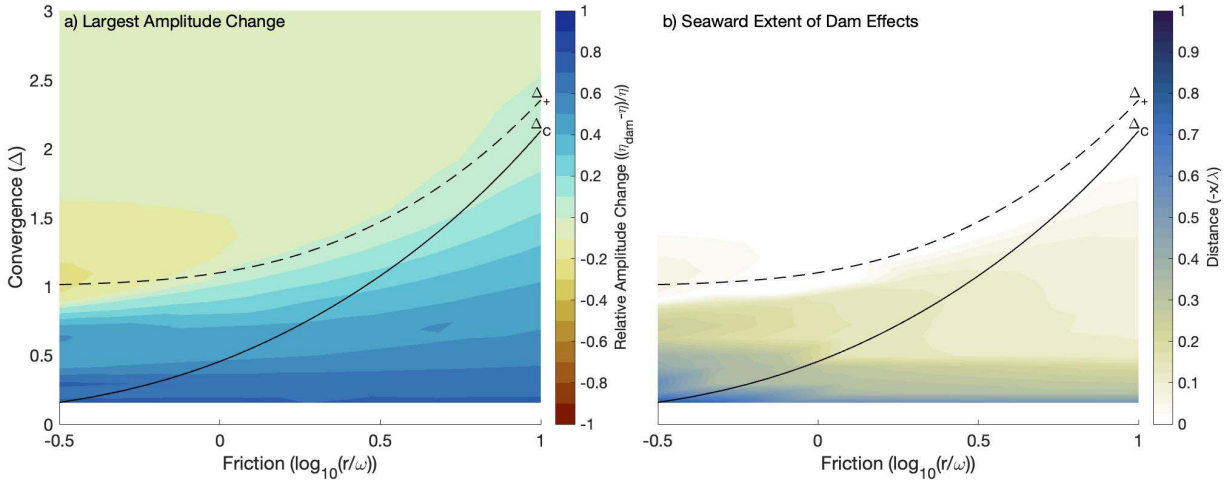

Figure 10. Modeled dam effects of a) the largest amplitude change and b) the seaward extent of dam effects, shown in friction-convergence parameter space. a) The line where shortening an estuary with a dam does not affect amplitudes is shown in black. b) The seaward extent of dam effects are defined as the maximum distance over which total amplitude changes were within an order of magnitude of the pre dam model (i.e., $|d\eta|>0.1\eta$).

The variable responses in amplitude is a result of constructive interference peaking at Δ_+, which occurs when incident and reflected wave phases are the same. The reflected wave, composed of only partial reflection from funneling, increases in amplitude and phase with the addition of dam reflection (Figure 8). For convergence $\Delta<\Delta_+$, amplification of the reflected wave with the addition of dam reflection increases the wave constructive interference (between incident and reflected wave) *more* than the increased phase difference reduces it. In the case of hyper-convergence $\Delta>\Delta_+$, on the contrary, dam amplification of the reflected wave increases constructive interference *less* than the increased phase difference reduces it. In the context of wave types, dam amplification could simultaneously be large for overtides and irrelevant for setup-setdown.

The spatial extent of dam influence on wave amplitude decreases seaward and extends a distance seaward that reduces with convergence and friction (Figure 10b). We quantify the spatial extent as the seaward distance amplitude changes in Figure 10a are within one order of magnitude (i.e., $|d\eta_d|>0.1$). We normalize results using the inviscid wavelength (i.e., $\lambda=T\sqrt{gh}$). Overall, the reflected wave propagates farthest in weakly convergent estuaries (small $\Delta\sim\lambda/L_a$); hence, the zone of reflection influence scales inversely with convergence. Seaward propagation of reflection effects is also farthest in weakly dissipative estuaries and is reduced by friction. For

the strongly and weakly convergent regimes (i.e., $\Delta<\Delta_+$), most variability scales with the e-folding length of landward funneling (L_a). Where also dissipative (i.e., $1<\frac{r}{\omega}<10$), the zone of influence is *~$1L_a$-$1.5L_a$*. Our reflection zone of influence is similar to the weakly convergent estuary estimate of Friedrichs (2010; ~L_a) and much larger than van Rijn (2011; ~$L_a/3$) van Rijn, 2011). Due to convergence effects (e.g., proximity to Δ_+), in the strongly convergent regime ($\Delta_C<\Delta<\Delta_+$), the seaward extent of dam effects counterintuitively increases with friction. While this is an interesting finding, the parameter space where dams most strongly amplify waves and affect the largest zone of influence are in the lower left, where convergence and friction are both weak (Figure 10a, b). In the parameter space shaded dark blue (Figure 10a), dams can nearly double long wave amplitudes. Further, reflection effects extend as far seaward as the wavelength itself, which in most estuaries would be the entire system.

The convergence parameter Δ affects long wave amplitudes in markedly different ways close to a dam than in more seaward regions (Figures 3a, 10a). Amplification from convergence occurs when $\Delta>\Delta_C$ and from dams occurs when $\Delta<\Delta_+$, allowing amplification to be summarized according to our three regimes (Figure 9): 1) hyper-convergent, where amplification is from only convergence ($\Delta>\Delta_+$, white), 2) weakly convergent, where amplification is from only dams ($\Delta<\Delta_C$, dark gray), and 3) strongly convergent, where amplification is from convergence and dams ($\Delta_C<\Delta<\Delta_+$, light gray). In seaward regions, amplification from a dam may be minimal (e.g., x_{dam}-$x>L_a$).

From the classifications introduced into Figure 9, general patterns are deduced. For systems with dominant tides in the strongly convergent regime, such as the Cooper River (Figure 3b):

- dominant tides amplify from convergence and dams
- storm surge is likely to be in the hyper-convergent regime—like setup-setdown waves—causing it to amplify with convergence but not dams (Figures 9, 10)
- overtides and other waves with a 4–8 hour period are in the weakly convergent regime, where waves attenuate landward because frictional dissipation exceeds amplification from convergence. But, such waves amplify in the landward direction near dams. The overtide effects scale inversely with period and are supported by observations showing M6 had stronger landward attenuation than M4 where dams were not present (i.e., Ashley and Wando Rivers) and stronger amplification when a dam was present (i.e., Cooper River; Figures 6,

S6). We note again that overtides are also strongly influenced by M2 overtide production, and the overall frictional environment set by tides and other waves (Parker, 2007).

Dam impacts may further change through time due to channel modifications and be predictable using the parameter space. For example, dredging deepens a system, shifting waves up and to the left in ($\frac{r}{\omega}$, Δ) parameter space. Localized changes may increase funneling, such as dredging predominantly in seaward regions or land reclamation of inland regions, shifting waves up in parameter space. These common changes, along with shortening from dams, describe the Ems and Guadalquivir River estuaries (Figure 3b; Chernetsky et al. 2010; Díez-Minguito et al., 2012; Ensing & de Swart 2015; Ruiz et al., 2015; Talke & Jay, 2020). Over time, the dominant semidiurnal tidal wave in the Ems shifted from the weakly convergent regime to the strongly convergent regime, near Δ_+. The parameter space change suggests that modern funneling amplification is much larger while dam amplification has moderately decreased. From a different historical parameter space location, the same shift for longer period waves—such as storm surges—may have decreased flooding risks, while the same shift for short period overtides may have greatly increased the seaward distance of dam amplification, further contributing to their sediment transport and fluid mud problems (Dijkstra et al., 2019). On the Hudson River, New York, navigational dredging of inland regions approaching the dam have reduced both convergence and friction, shifting the region down-left in parameter space and explaining the larger modern amplitudes near the dam (Ralston et al., 2018). Similar changes on the Cooper River and Tombigbee River, where storm surge is also observed reflecting, suggest dredging navigational channels to dams compounds dam effects, increasing dam amplification and the region affected.

6.3 Broader Impacts of Dams

The implication of dams on secondary processes like salt intrusion, sediment transport, and ecological impacts are motivations for their constructions (e.g., salt barrages). Studies of dam effects almost exclusively focus on processes associated with the dominant tides without quantify the magnitude of dam reflection (e.g., Arunpandi et al., 2022; Figueroa et al., 2022; Kidd et al., 2017). Observational results can appear to conflict—with strong dam associated effects in some estuaries and none in others (Prandle & Rahman, 1980)—likely caused by focusing on processes related to a range of waves and systems in different parameter spaces. Modeling studies like Figueroa et al. (2022) carefully cover a wide range of estuarine circulation

parameter space (i.e., mixing number vs freshwater Froude number; Geyer & McCready, 2014) but their geometry and semidiurnal waves follow a Regional Ocean Model default case that place their study in an extreme region of our friction-convergence parameter space (L_a>3, Δ>10). Their results show circulation changes are strongly affected by dam regulations of river discharge, supporting our interpretations about elevated friction, but do so using extreme ranges (e.g., U_r/U_t~0.004–3). Similarly, Du et al. (2018) call L_a=60km 'strongly convergent' and model a narrow range of low convergence (Δ<0.45), concluding length is the key factor determining how estuaries respond to sea level rise. However, we show length becomes less critical as convergence increases and negligible as $\Delta >> \Delta_+$ (e.g., Figure 10b). Future studies of dam effects on secondary processes might be improved by identifying where primary effects from different wave types (not just M2) are in the friction-convergence parameter space (Figures 3, 9, 10).

As the number of dams in marine environments continues to grow (Figueroa et al., 2022; Tilai et al., 2019), engineers and managers should consider the potential effects associated with all wave forms. Kidd et al. (2017) argue that the regulation of secondary processes such as salinity intrusion by estuarine dams do not outweigh the costs and are often counterproductive. Our results suggest that storm surge amplification can occur from convergence and dams; hence, the influence of a dam on flood hazard should be considered. Systems traditionally identified as weakly convergent for dominant tides likely have some storm surge events that strongly amplify due to funneling (i.e., are near Δ_+); other storm surge events in the same estuary may be in the weakly convergent regime and are at risk for amplification from dams. Because funneling often decreases in tidal rivers towards a constant width channel (e.g., Jay & Flinchem, 1997), the reflection effects in this small Δ regime may be larger than further seaward. Further, long period waves (such as the 2 day surge considered here) may be most influenced, as the distance waves propagate inland scales with wave period (Jay & Flinchem, 1997). Even beyond the head of tides, longer period waves may reflect off dams and increase flood risk (e.g., Dykstra & Dzwonkowski, 2021). For managing traditionally hyper-convergent estuaries, dam effects may be overlooked as they may only intensify short period overtides and transport patterns. New and proposed barriers (e.g., for the Hudson River; Ralston, 2022) need to consider how the distance landward may interact with the local geometry for a range of surge and tidal conditions or compound storm tides. Lastly, management plans may need flexibility as dam amplification could also oscillate with natural variability, such as tidal cycles (e.g., spring-neap, Lunar node),

river flows, meteorological forcing, and seasonality (e.g., ice; Georges 2012, Wang et al., 2012), or change through time from humans directly impacting the geometry or sea level rise extending marine processes landward.

7 Conclusions

The effects of shortening an estuary with a dam on tides and storm surge in naturally convergent and modified systems are investigated using a case study of Charleston Harbor. We use observational data, compare it to theory with a 1-dimentioinal semi-analytical model, and evaluate and explain the dynamical response using a friction-convergence parameter space. The Cooper River dam and geomorphic funneling produce full and partial reflections, respectively, with different effects depending on whether the long wave was tidal, storm surge, or setup-setdown in nature. While both partial and full reflections propagate seaward, the critical difference is apparent in their opposite longitudinal trends. Funneling induced partial reflections are cumulative—with an overall signal that is phase-locked to incident waves—and exhibit a *landward* phase increase and amplitude decrease. The dam induced full reflections are characterized by a *seaward* phase increase and amplitude decrease (Figure 8c–f). The primary conclusions are:

1. Convergence Δ—which we define as the ratio of wavelength to geomorphic funneling—is the most important factor controlling amplification in a dammed frictional estuary, followed by friction.
2. For a given friction $\frac{r}{\omega}$, funneling effects maximize wave amplitude and celerity when friction, convergence, and acceleration cause the complex wavenumber to approach zero (wavelength approach infinity), a condition at which we delineate Δ_+.
3. Dam reflection (full reflection) can increase or decrease constructive interference; reflection from a barrier amplifies waves when convergence is weak $\Delta<\Delta_+$ and attenuates waves when convergence is strong $\Delta>\Delta_+$.
4. The friction-convergence parameter space reveals that the convergence and dam effects on estuarine long waves have distinctive dynamics which fall into three different regimes: weakly convergent, strongly convergent, and hyper-convergent.
5. Storm surge can straddle different regimes in the friction-convergence parameter space, depending on the period and amplitude of the event and local geometric characteristics.

Because dominant tides are often near critical convergence (Figure 3b), the most likely location in the parameter space for storm surge is the hyper-convergent regime with minimal amplitude variability. However, for large amplitude, short duration events or weakly funneling estuaries, storm surge may be in the weakly convergent regime and amplify at a reflection point. Thus, the characteristics of events that cause a flood hazard at a dam should be carefully considered with respect to the parameter space. In some estuaries, the most intense storm surge may occur near dams.

6. For Charleston—due to the strong landward funneling—flood risks associated with tide and storm surge are shown in observations and modeling to be localized to the upper Cooper River. However, if proposed dredging were extended inland, dam amplification may increase and cause amplified water levels further seaward. For other systems, researchers and managers will be aided by using the presented parameter space to approximate how funneling and dams affect estuarine processes and flooding risks, both now and under future changes from human development and sea level rise.

Acknowledgments, Samples, and Data

This research was funded through the University of South Carolina Advanced Support Program for Innovative Research Excellence-II and the National Science Foundation (RISE 2013280, CBET 1751926). We would like to thank our field assistants (Mahsa Ahmadpoor, Shailesh van der Steeg, Samantha Pollack, Kyle Gradzki), Todd Ehret for completing the NOAA data request, and others for insightful discussions (David Jay, Parker MacCready, Philip Orton, Stephen Figueroa, Olivia Szot). We are unaware of any perceived financial conflicts of interests or affiliations.

Open Research

All data needed to recreate this analysis are publicly available through the NOAA (Tides & Currents: https://tidesandcurrents.noaa.gov/, Mobile, Alabama DEM: https://www.ncei.noaa.gov/access/metadata/landing-page/bin/iso?id=gov.noaa.ngdc.mgg.dem:671), the USGS (National Water Information System: https://waterdata.usgs.gov/nwis), the National Estuary Research Reserve (IOOS:

https://sensors.ioos.us/#metadata/75585/station/data), CIRES (2014), and Dykstra et al. (2022b, 2022c). Individual stations are further detailed in Table S1 of the Supplementary Information.

References

Althausen, J. D., & Kjerfve, B. (1992). Distribution of suspended sediment in a partially mixed estuary, Charleston Harbor, South Carolina, USA. *Estuarine, Coastal and Shelf Science*. https://doi.org/10.1016/s0272-7714(05)80028-9

Army Corp of Engineers (2015). Charleston Harbor Post 45: Final integrated feasibility report and environmental impact statement.

Arunpandi, N., Jyothibabu, R., Jagadeesan, L., Arya, P. M., Rashid, C. P., & Sarath, S. (2022). Response of smaller plankton to the saltwater barrage-altered hydrography of a tropical estuarine system on India's southwest coast. *Ocean & Coastal Management*, *226*, 106257. https://doi.org/10.1016/j.ocecoaman.2022.106257

Battjes, J. A., Labuer, R. J. (2014). *Open Channel Flow*. TU Delft: 06917290048.

Bosserelle, A. L., Morgan, L. K., & Hughes, M. W. (2022). Groundwater Rise and Associated Flooding in Coastal Settlements Due To Sea-Level Rise: A Review of Processes and Methods. *Earth's Future*, *10*(7). https://doi.org/10.1029/2021ef002580

Buschman, F. A., Hoitink, A. J. F. T., Vegt, M. van der, & Hoekstra, P. (2009). Subtidal water level variation controlled by river flow and tides. *Water Resources Research*, *45*(10), 7715–12. https://doi.org/10.1029/2009wr008167

Cooperative Institute for Research in Environmental Sciences (CIRES) at the University of Colorado, Boulder (2014). Continuously Updated Digital Elevation Model (CUDEM) - 1/9 Arc-Second Resolution Bathymetric-Topographic Tiles. NOAA National Centers for Environmental Information. https://doi.org/10.25921/ds9v-ky35. Accessed 2021

Díez-Minguito, M., Baquerizo, A., Ortega-Sanchez, M., Navarro, G., & Losada, M. A. (2012). Tide transformation in the Guadalquivir estuary (SW Spain) and process-based zonation. *Journal of Geophysical Research*, *117*(C3), 1–14. https://doi.org/10.1029/2011jc007344

Dijkstra, Y. M., Schuttelaars, H. M., Schramkowski, G. P., & Brouwer, R. L. (2019). Modeling the Transition to High Sediment Concentrations as a Response to Channel Deepening in the Ems River Estuary. *Journal of Geophysical Research: Oceans*, *124*(3), 1578–1594. https://doi.org/10.1029/2018jc014367

Du, J., Shen, J., Zhang, Y. J., Ye, F., Liu, Z., Wang, Z., et al. (2018). Tidal Response to Sea-Level Rise in Different Types of Estuaries: The Importance of Length, Bathymetry, and Geometry. *Geophysical Research Letters*, *45*(1), 227–235. https://doi.org/10.1002/2017gl075963

Dykstra, S. L., & Dzwonkowski, B. (2021). The Role of Intensifying Precipitation on Coastal River Flooding and Compound River-Storm Surge Events, Northeast Gulf of Mexico. *Water Resources Research*, *57*(11). https://doi.org/10.1029/2020wr029363

Dykstra, S. L., Dzwonkowski, B., & Torres, R. (2022). The role of river discharge and geometric structure on diurnal tidal dynamics, Alabama, USA. *Journal of Geophysical Research: Oceans*. https://doi.org/10.1029/2021jc018007

Dykstra, S. L., & Dzwonkowski, B. (2020). The propagation of fluvial flood waves through a backwater-estuarine environment. *Water Resources Research*, *56*(2), e25743. https://doi.org/10.1029/2019wr025743

1013 Dykstra, S. L., R. Torres, E. Viparelli, S. A. Talke, A. E. Yankovsky (2022). Historical Water
1014 Level Data of the Greater Charleston Region (1975-1992), Previously Unpublished by
1015 NOAA, HydroShare,
1016 http://www.hydroshare.org/resource/6426732916294b03950d5cc9ca15b252
1017 Dykstra, S. L., R. Torres, E. Viparelli, S. Talke, A. E. Yankovsky (2022). Water Level and
1018 Temperature Data of the Greater Charleston Region (Ashley, Cooper, and Wando Rivers),
1019 Field Collected 2021 May-November,
1020 HydroShare, http://www.hydroshare.org/resource/87a32300574b4489b1716d5ed058c085
1021 Ensign, S. H., & Noe, G. B. (2018). Tidal extension and sea-level rise: recommendations for a
1022 research agenda. *Frontiers in Ecology and the Environment*, *16*(1), 37–43.
1023 https://doi.org/10.1002/fee.1745
1024 Faden, W., Bull, W., De Brahm, J. G. W. & Stuart, J. (1780) *A map of South Carolina and a part*
1025 *of Georgia*. London. Retrieved from the Library of Congress,
1026 https://www.loc.gov/item/74692514/.
1027 Figueroa, S. M., Lee, G., Chang, J., & Jung, N. W. (2022). Impact of Estuarine Dams on the
1028 Estuarine Parameter Space and Sediment Flux Decomposition: Idealized Numerical
1029 Modeling Study. *Journal of Geophysical Research: Oceans*, *127*(5).
1030 https://doi.org/10.1029/2021jc017829
1031 Friedrichs, C. T., & Aubrey, D. G. (1994). Tidal propagation in strongly convergent channels.
1032 *Journal of Geophysical Research*.
1033 Friedrichs, C. T., Armbrust, B. A., & Swart, H. E. de. (1998). Hydrodynamics and equilibrium
1034 sediment dynamics of shallow, funnel-shaped tidal estuaries. In *VIMS Books and Book*
1035 *Chapters* (Vol. 38). Retrieved from https://scholarworks.wm.edu/vimsbooks/38
1036 Gallo, M. N., & Vinzon, S. B. (2005). Generation of overtides and compound tides in Amazon
1037 estuary. *Ocean Dynamics*, *55*(5–6), 441–448. https://doi.org/10.1007/s10236-005-0003-8
1038 Georgas, N. (2012). Large Seasonal Modulation of Tides due to Ice Cover Friction in a
1039 Midlatitude Estuary*. *Journal of Physical Oceanography*, *42*(3), 352–369.
1040 https://doi.org/10.1175/jpo-d-11-063.1
1041 Godin, G. (1999). The Propagation of Tides up Rivers With Special Considerations on the Upper
1042 Saint Lawrence River. *Estuarine, Coastal and Shelf Science*, *48*(3), 307–324.
1043 https://doi.org/10.1006/ecss.1998.0422
1044 Hoeksema, R. J. (2006). Designed for dry feet: Flood protection and land reclamation in the
1045 Netherlands. American Society of Civil Engineers.
1046 Jay, D. A. (1991). Green's law revisited: Tidal long-wave propagation in channels with strong
1047 topography. *Journal of Geophysical Research: Oceans*, *96*(C11), 20585–20598.
1048 https://doi.org/10.1029/91jc01633
1049 Jay, D. A., & Flinchem, E. P. (1997). Interaction of fluctuating river flow with a barotropic tide:
1050 A demonstration of wavelet tidal analysis methods. *Journal of Geophysical Research*.
1051 https://doi.org/10.1029/96jc00496/full
1052 Kästner, K., Hoitink, A. J. F. T., Torfs, P. J. J. F., Deleersnijder, E., & Ningsih, N. S. (2019).
1053 Propagation of tides along a river with a sloping bed. *Journal of Fluid Mechanics*, *872*, 39–
1054 73. https://doi.org/10.1017/jfm.2019.331
1055 Kidd, I. M., Davis, J. A., & Fischer, A. (2017). Total exclusion barrages as sea-level rise
1056 mitigators: The geomorphological trade-offs for new installations. *Ocean & Coastal*
1057 *Management*, *143*, 122–135. https://doi.org/10.1016/j.ocecoaman.2016.08.012

1058 Kjerfve, B., & Magill, K. E. (1990). Salinity Changes in Charleston Harbor 1922-1987. *Journal*
1059 *of Waterway, Port, Coastal, and Ocean Engineering*, *116*(2), 153–168.
1060 https://doi.org/10.1061/(asce)0733-950x(1990)116:2(153)
1061 Kukulka, T., & Jay, D. A. (2003). Impacts of Columbia River discharge on salmonid habitat: 1.
1062 A nonstationary fluvial tide model. *Journal of Geophysical Research*, *108*(C9), 1–20.
1063 https://doi.org/10.1029/2002jc001382
1064 Lanzoni, S., & Seminara, G. (1998). On tide propagation in convergent estuaries. *Journal of*
1065 *Geophysical Research: Oceans*, *103*(C13), 30793–30812.
1066 https://doi.org/10.1029/1998jc900015
1067 Lee, S. B., Li, M., & Zhang, F. (2017). Impact of sea level rise on tidal range in Chesapeake and
1068 Delaware Bays. *Journal of Geophysical Research: Oceans*, *122*(5), 3917–3938.
1069 https://doi.org/10.1002/2016jc012597
1070 Leo, F., Talke, S. A., Orton, P. M., & Wahl, T. (2022). The Effect of Harbor Developments on
1071 Future High-Tide Flooding in Miami, Florida. *Journal of Geophysical Research: Oceans*,
1072 *127*(7). https://doi.org/10.1029/2022jc018496
1073 Lighthill, M. J. (1978). *Waves in fluids*. Cambridge university press.
1074 Morris, K. A. R. J. T. (2020). Past, present, and future nuisance flooding on the Charleston
1075 peninsula, 1–16. https://doi.org/10.1371/journal.pone.0238770
1076 Morse, B., Ringô, B., Messier, D., Thanh-Quach, T., & Stander, E. (2006). Hydrodynamics of
1077 Mesotidal Estuary in Winter. *Journal of Cold Regions Engineering*, *20*(3), 95–115.
1078 https://doi.org/10.1061/(asce)0887-381x(2006)20:3(95)
1079 Prandle, D., & Rahman, M. (1980). Tidal Response in Estuaries. *Journal of Physical*
1080 *Oceanography*, *10*(10), 1552–1573.
1081 Proudman, J. (1955). The propagation of tide and surge in an estuary. *Proceedings of the Royal*
1082 *Society of London. Series A. Mathematical and Physical Sciences*, *231*(1184), 8–24.
1083 https://doi.org/10.1098/rspa.1955.0153
1084 Ralston, D. K. (2022). Impacts of Storm Surge Barriers on Drag, Mixing, and Exchange Flow in
1085 a Partially Mixed Estuary. *Journal of Geophysical Research: Oceans*, *127*(4).
1086 https://doi.org/10.1029/2021jc018246
1087 Ralston, D. K., Talke, S. A., Geyer, W. R., Al'Zubadaei, H., & Sommerfield, C. K. (2018).
1088 Bigger tides, less flooding: Effects of dredging on barotropic dynamics in a highly modified
1089 estuary. *Journal of Geophysical Research: Oceans*, 2018JC014313-16.
1090 https://doi.org/10.1029/2018jc014313
1091 Rijn, L. C. van. (2011). Analytical and numerical analysis of tides and salinities in estuaries; part
1092 I: tidal wave propagation in convergent estuaries. *Ocean Dynamics*, *61*(11), 1719–1741.
1093 https://doi.org/10.1007/s10236-011-0453-0
1094 Rojas, I. J., Sottolichio, A., Hanquiez, V., Fort, A., & Schmidt, S. (2018). To What Extent
1095 Multidecadal Changes in Morphology and Fluvial Discharge Impact Tide in a Convergent
1096 (Turbid) Tidal River. *Journal of Geophysical Research: Oceans*, *123*(5), 3241–3258.
1097 https://doi.org/10.1002/2017jc013466
1098 Ruiz, J., Polo, M. J., Díez-Minguito, M., Navarro, G., Morris, E. P., Huertas, E., et al. (2014).
1099 Environmental Management and Governance, Advances in Coastal and Marine Resources.
1100 *Coastal Research Library*, 199–232. https://doi.org/10.1007/978-3-319-06305-8_8
1101 Schumann, E. H., & Brink, K. H. (2009). Tidal and subtidal water level fluctuations in the Berg
1102 Estuary. *Transactions of the Royal Society of South Africa*, *64*(2), 181–188.
1103 https://doi.org/10.1080/00359190909519251

1104 Schuttelaars, H. M., & Swart, H. E. (2000). Multiple morphodynamic equilibria in tidal
1105 embayments. *Journal of Geophysical Research: Oceans*, *105*(C10), 24105–24118.
1106 https://doi.org/10.1029/2000jc900110
1107 Sohrt, V., Hein, S. S. V., Nehlsen, E., Strotmann, T., & Fröhle, P. (2021). Model Based
1108 Assessment of the Reflection Behavior of Tidal Waves at Bathymetric Changes in Estuaries.
1109 *Water*, *13*(4), 489. https://doi.org/10.3390/w13040489
1110 Spicer, P., Huguenard, K., Ross, L., & Rickard, L. N. (2019). High-frequency tide-surge-river
1111 interaction in estuaries: causes and implications for coastal flooding. *Journal of Geophysical*
1112 *Research: Oceans*, *124*(12), 9517–9530. https://doi.org/10.1029/2019jc015466
1113 Swart, H. E. de, & Zimmerman, J. T. F. (2009). Morphodynamics of Tidal Inlet Systems. *Annual*
1114 *Review of Fluid Mechanics*, *41*(1), 203–229.
1115 https://doi.org/10.1146/annurev.fluid.010908.165159
1116 Sweet WV, Park J, From the extreme to the mean: Acceleration and tipping points of coastal
1117 inundation from sea level rise. Earth's Future 2014; 2: 579–600,
1118 https://doi.org/10.1002/2014EF000272
1119 Szot, O. & Dykstra, S. L. (2022). Longitudinal DEM Tool for the Extraction of River and
1120 Estuary Cross Sections. Published by GitHub, inc.
1121 https://github.com/onszot/longitudinal_DEM
1122 Talke, Stefan A, & Jay, D. A. (2020). Changing Tides: The Role of Natural and Anthropogenic
1123 Factors. *Annual Review of Marine Science*, *12*(1), 121–151. https://doi.org/10.1146/annurev-
1124 marine-010419-010727
1125 Talke, Stefan A, Orton, P., & Jay, D. A. (2014). Increasing storm tides in New York Harbor,
1126 1844-2013. *Geophysical Research Letters*, *41*(9), 3149–3155.
1127 https://doi.org/10.1002/2014gl059574
1128 Talke, Stefan A, Kemp, A. C., & Woodruff, J. (2018). Relative Sea Level, Tides, and Extreme
1129 Water Levels in Boston Harbor From 1825 to 2018. *Journal of Geophysical Research:*
1130 *Oceans*, *123*(6), 3895–3914. https://doi.org/10.1029/2017jc013645
1131 Tilai, L., Liming, C., Xiangyu, G., & Lei, D. (2019). APAC 2019, Proceedings of the 10th
1132 International Conference on Asian and Pacific Coasts, 2019, Hanoi, Vietnam, 649–655.
1133 https://doi.org/10.1007/978-981-15-0291-0_89
1134 U.S. Department of Commerce (1989). Charleston Harbor: Issues, Resources, Status, and
1135 Management. *NOAA Estuary-of-the-Month Seminar Series* (Vol. 16, pp. 13-24)
1136 van Veen, J. (1962). Dredge, Drain, and Reclaim: The Art of a Nation, 1st edition The Hague:
1137 Martinus Nijhoff. Talke, S. A., Familkhalili, R., & Jay, D. A. (2021). The Influence of
1138 Channel Deepening on Tides, River Discharge Effects, and Storm Surge. *Journal of*
1139 *Geophysical Research: Oceans*, *126*(5). https://doi.org/10.1029/2020jc016328
1140 Wang, R., McCullough, G. K., Gunn, G. G., Hochheim, K. P., Dorostkar, A., Sydor, K., &
1141 Barber, D. G. (2012). An observational study of ice effects on Nelson River estuarine
1142 variability, Hudson Bay, Canada. *Continental Shelf Research*, *47*, 68–77.
1143 https://doi.org/10.1016/j.csr.2012.06.014
1144 Webster, I. T. (2010). The hydrodynamics and salinity regime of a coastal lagoon – The
1145 Coorong, Australia – Seasonal to multi-decadal timescales. *Estuarine, Coastal and Shelf*
1146 *Science*, *90*(4), 264–274. https://doi.org/10.1016/j.ecss.2010.09.007
1147 Winterwerp, J. C., & Wang, Z. B. (2013). Man-induced regime shifts in small estuaries—I:
1148 theory. *Ocean Dynamics*, *63*(11–12), 1279–1292. https://doi.org/10.1007/s10236-013-0662-9

Wright, L. D., Coleman, J. M., & Thom, B. G. (1973). Processes of Channel Development in a High-Tide-Range Environment: Cambridge Gulf-Ord River Delta, Western Australia. *The Journal of Geology*, *81*(1), 15–41. https://doi.org/10.1086/627805

Yankovsky, A. E., & Iyer, S. K. (2015). Propagation of subtidal sea level oscillations in the river channel: A case study of the St. Johns River, Florida, USA. *Estuarine, Coastal and Shelf Science*, *157*, 69–78. https://doi.org/10.1016/j.ecss.2015.02.012

Zhang, T., & Yankovsky, A. E. (2016). On the nature of cross-isobath energy fluxes in topographically modified barotropic semidiurnal Kelvin waves. *Journal of Geophysical Research: Oceans*, *121*(5), 3058–3074. https://doi.org/10.1002/2015jc011617

Figure1.

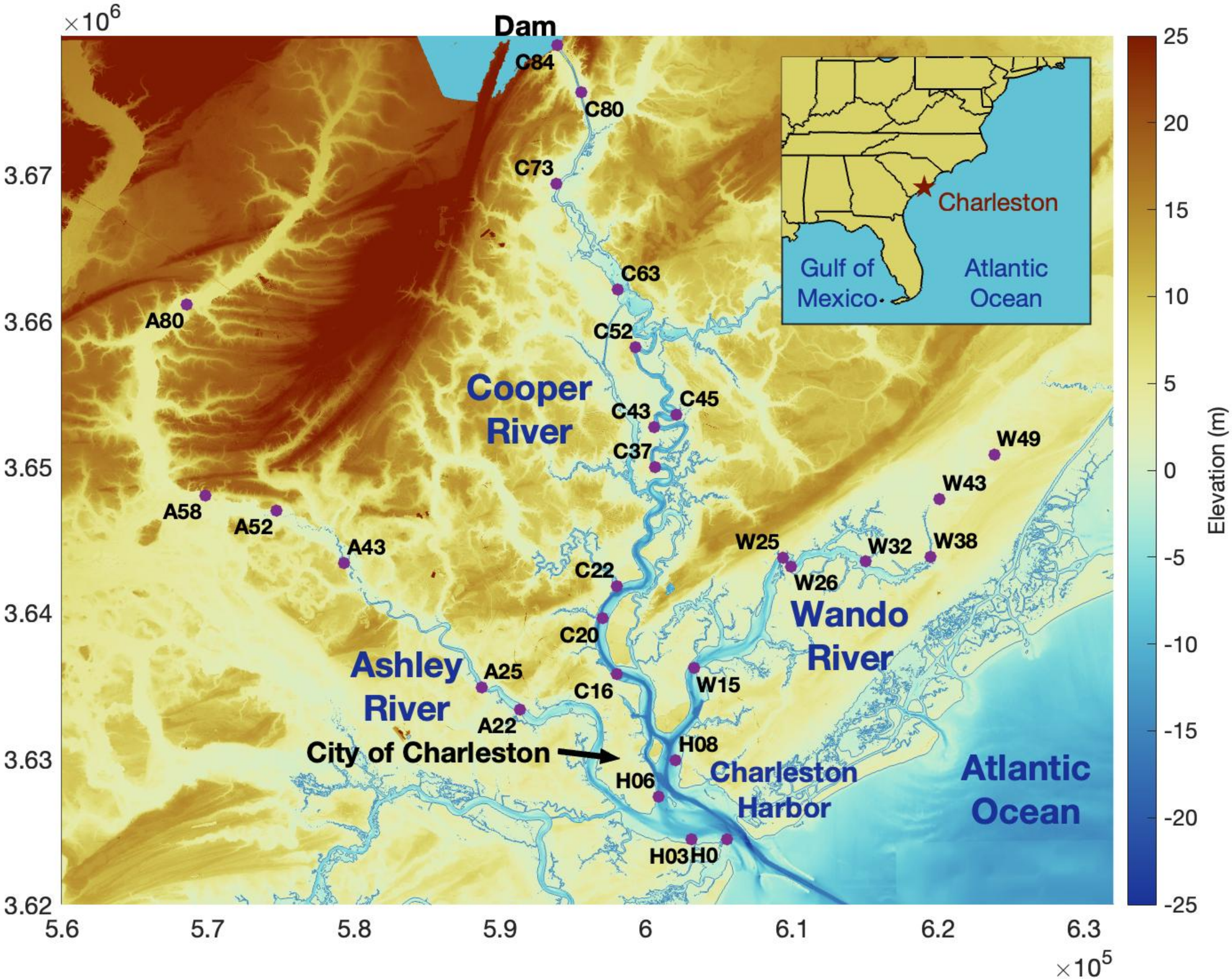
×10^6
3.67
3.66
3.65
3.64
3.63
3.62
5.6
5.7
5.8
5.9
6
6.1
6.2
6.3
×10^5
Dam
C84
C80
C73
C63
C52
C45
C43
C37
C22
C20
C16
A80
A58
A52
A43
A25
A22
H08
H06
H03
H0
W49
W43
W38
W32
W25
W26
W15
Cooper River
Ashley River
City of Charleston
Wando River
Charleston Harbor
Atlantic Ocean
Charleston
Gulf of Mexico
Atlantic Ocean
Elevation (m)
25
20
15
10
5
0
-5
-10
-15
-20
-25

Figure2.

a) Convergent Model Width

500
0
-500
Width (m)
Dam

b) Rectangle Model Width

Dam

c) Convergent Model Depth

0
-5
-10
Depth (m)
Dam

d) Rectangle Model Depth

Dam

e) Convergent Model Drag Coef.

$\times 10^{-3}$
5
0
Drag Coef.
Cd_r
Cd_t
0
20
40
60
80
Distance Inland (km)

f) Rectangle Model Drag Coef.

Cd_t
Cd_r
0
20
40
60
80
Distance Inland (km)

Figure3.

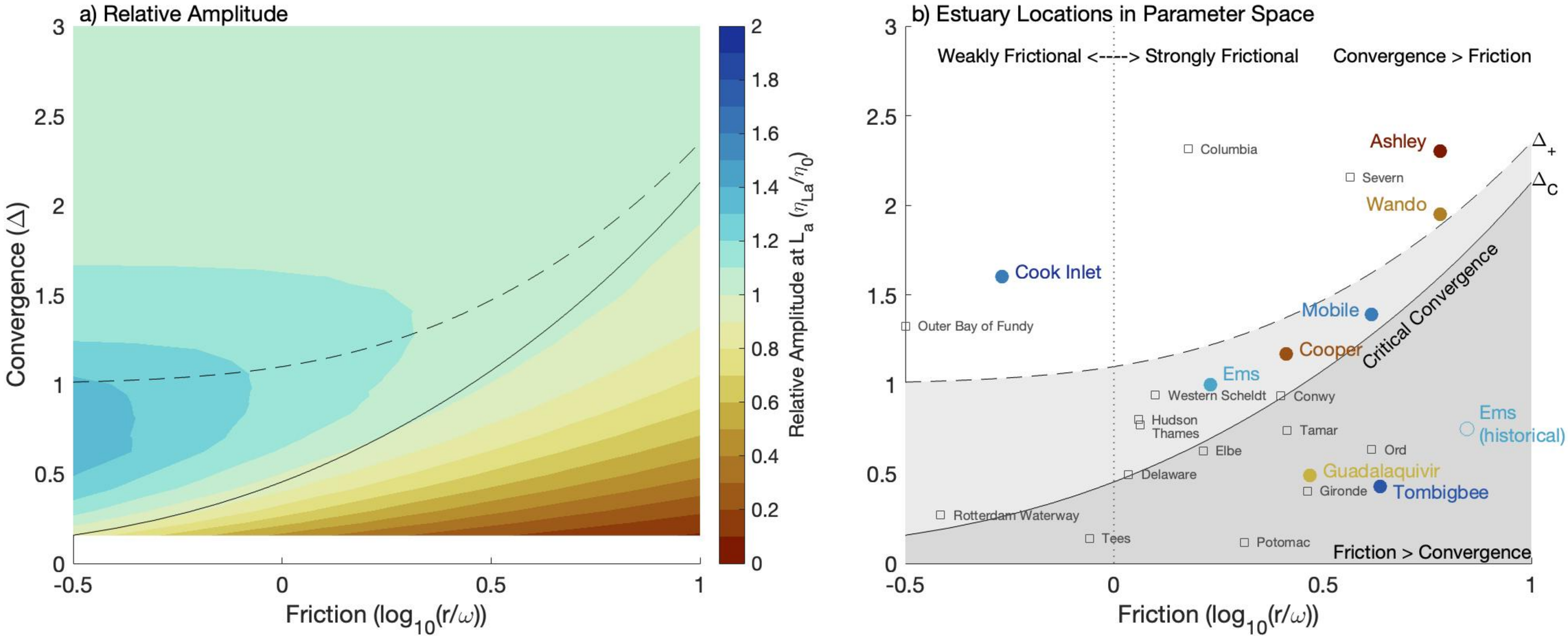
a) Relative Amplitude
Convergence (Δ)
Friction (log10(r/ω))
Relative Amplitude at La (ηLa/η0)
b) Estuary Locations in Parameter Space
Weakly Frictional <----> Strongly Frictional
Convergence > Friction
Friction > Convergence
Critical Convergence
Δ+
ΔC
Ashley
Wando
Cook Inlet
Mobile
Cooper
Ems
Ems (historical)
Guadalaquivir
Tombigbee
Columbia
Severn
Outer Bay of Fundy
Western Scheldt
Conwy
Hudson
Thames
Tamar
Elbe
Ord
Delaware
Gironde
Rotterdam Waterway
Tees
Potomac

Figure4.

a)

Area (m^2)

10^4

10^3

10^2

0 10 20 30 40 50 60 70 80

Distance Inland (km)

Ashley River
Cooper River
Wando River

L_a = 25.1km
L_a = 9.9km
L_a = 8.4km

b)

10^4

10^3

10^2

10^1

0 10 20 30 40 50 60 70 80

Distance Inland (km)

Cooper River Area (m^2)
Cooper River Width (m)
Cooper River Depth (m)

L_a = 25.1km
L_w = 35.0km
L_h = 90.5km

Figure5.

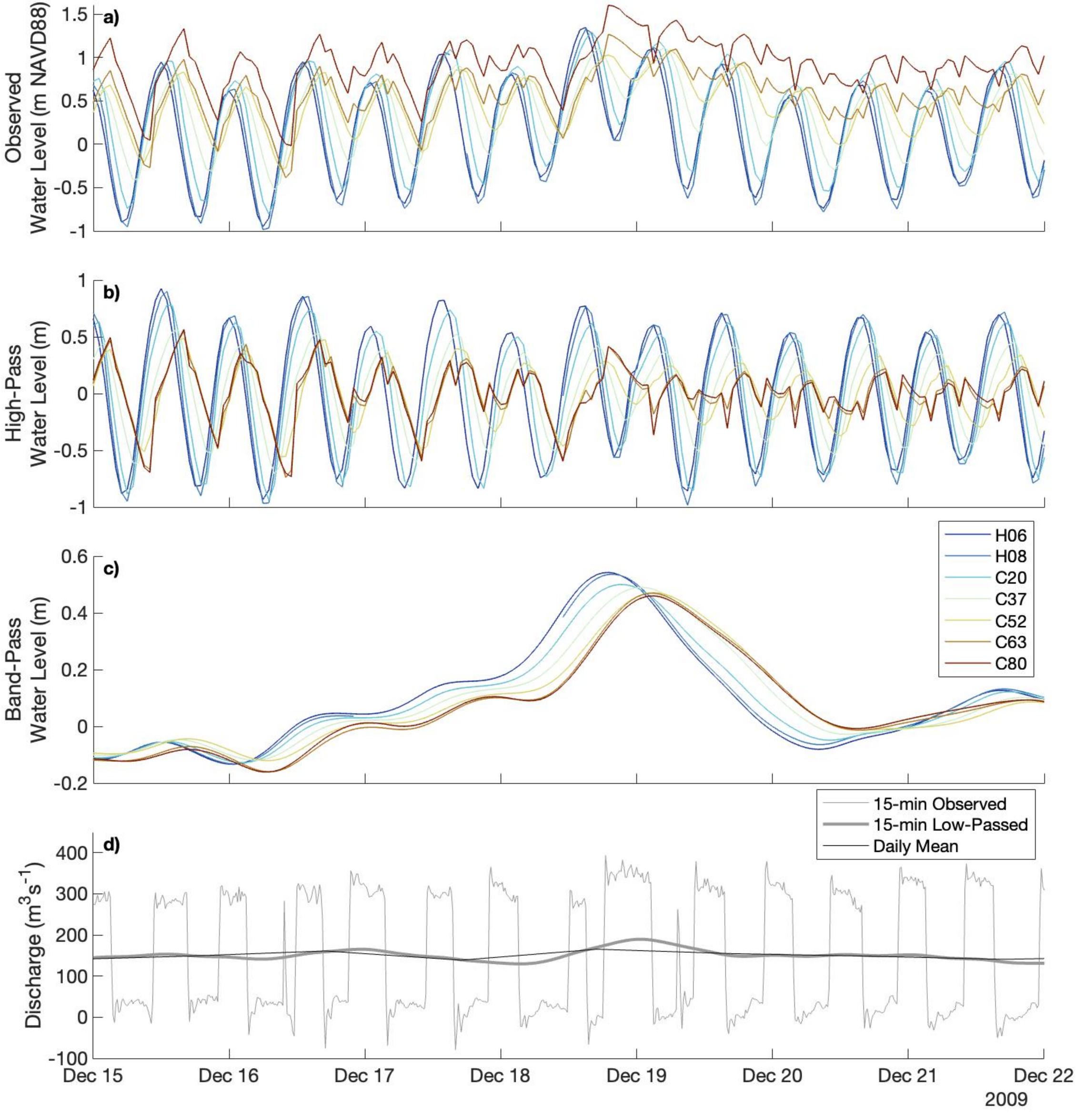
a)
Observed
Water Level (m NAVD88)
1.5
1
0.5
0
-0.5
-1
b)
High-Pass
Water Level (m)
1
0.5
0
-0.5
-1
c)
Band-Pass
Water Level (m)
0.6
0.4
0.2
0
-0.2
H06
H08
C20
C37
C52
C63
C80
d)
Discharge (m3s-1)
400
300
200
100
0
-100
15-min Observed
15-min Low-Passed
Daily Mean
Dec 15
Dec 16
Dec 17
Dec 18
Dec 19
Dec 20
Dec 21
Dec 22
2009

Figure6.

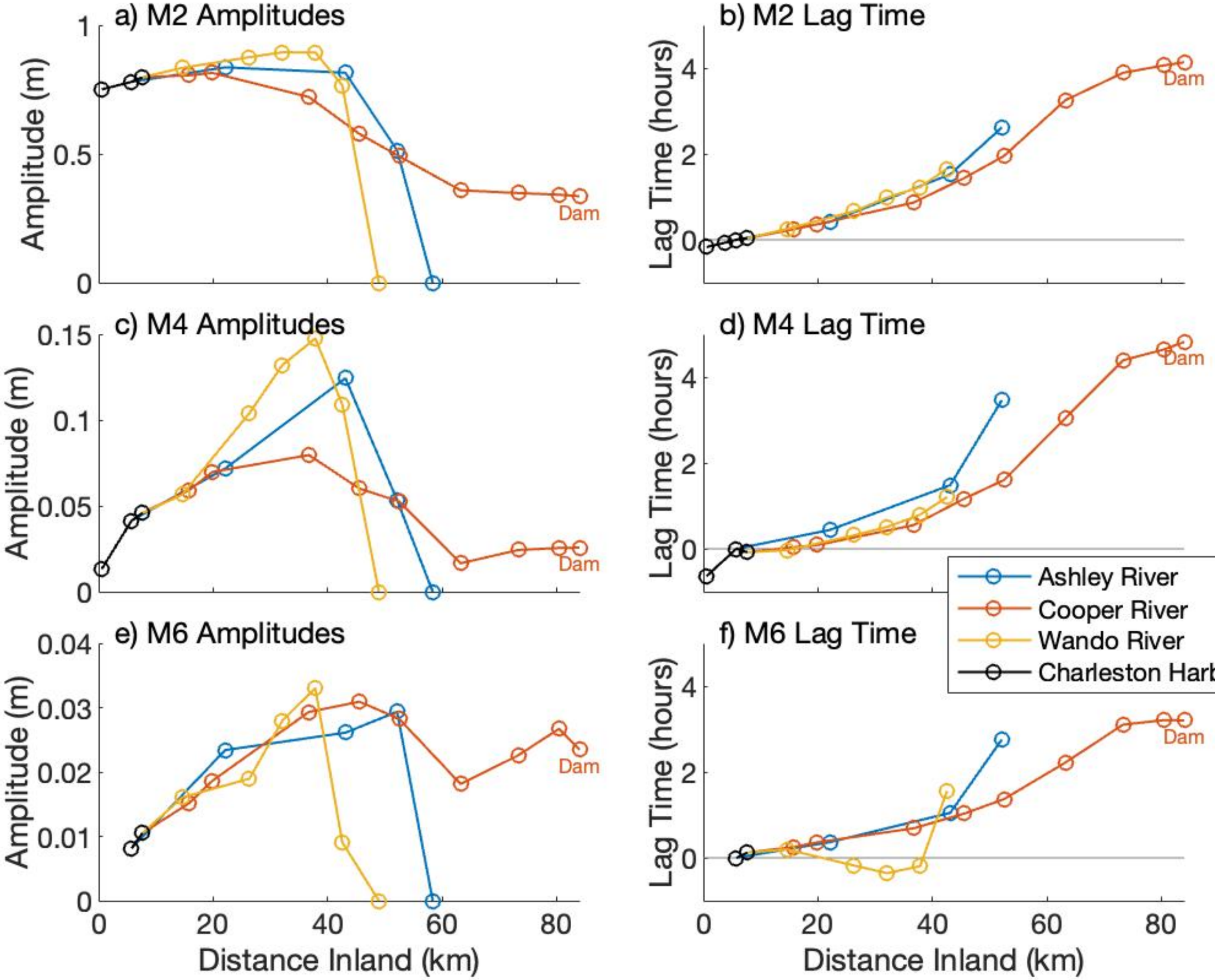
a) M2 Amplitudes
Amplitude (m)
1
0.5
0
Dam
b) M2 Lag Time
Lag Time (hours)
4
2
0
Dam
c) M4 Amplitudes
Amplitude (m)
0.15
0.1
0.05
0
Dam
d) M4 Lag Time
Lag Time (hours)
4
2
0
Dam
Ashley River
Cooper River
Wando River
Charleston Harbor
e) M6 Amplitudes
Amplitude (m)
0.04
0.03
0.02
0.01
0
Dam
0
20
40
60
80
Distance Inland (km)
f) M6 Lag Time
Lag Time (hours)
4
2
0
Dam
0
20
40
60
80
Distance Inland (km)

Figure7.

a) Setup-Setdown Magnitude

Relative Magnitude

1
0.8
0.6
0.4
0.2
0

Ashley River
Cooper River
Wando River

b) Setup-Setdown Lag Time

Lag Time (hours)

10
5
0

c) Storm Surge Height

Surge Height (m)

1
0.8
0.6
0.4
0.2
0

0
20
40
60
80

Distance Inland (km)

d) Storm Surge Lag Time

Lag Time (hours)

10
5
0

0
20
40
60
80

Distance Inland (km)

Figure8.

a) M2 Tidal Amplitudes: Total

b) Storm Surge Amplitudes: Total

Convergent-Dam
Convergent-No Dam
Nonconvergent-Dam

c) M2 Tidal Amplitudes: Inc. vs Ref.

d) Storm Surge Amplitudes: Inc. vs Ref.

Amplitude (m)
0
0.2
0.4
0.6
0.8

e) M2 Tidal Phases: Inc. vs Ref.

f) Storm Surge Phases: Inc. vs Ref.

Convergent-Dam
Convergent-No Dam
Nonconvergent-Dam
Incident Wave
Reflected Wave

Phase (degrees)
225
180
135
90
45
0

0
20
40
60
80
Distance Inland (km)

Figure9.

Setup-Setdown
Storm Surge
Mouth
Tide (r/ω: harmonic)
Tide (r/ω: estuary)
M2 Modeled
K1
K1
Δ_+
Δ_C
Convergence (Δ)
3
2.5
2
1.5
1
0.5
0
Hyper-Convergent:
Funneling Amplification
Dam Attenuation
M2
M2
Dam
M3
Strongly Convergent:
Funneling Amplification
Dam Amplification
M4
M4
M6
M8
Weakly Convergent:
Funneling Attenuation
Dam Amplification
rkm 70
Dam Effects: Regional
Dam Effects: Local
-0.5
0
0.5
1
Friction ($\log_{10}(r/\omega)$)

Figure10.

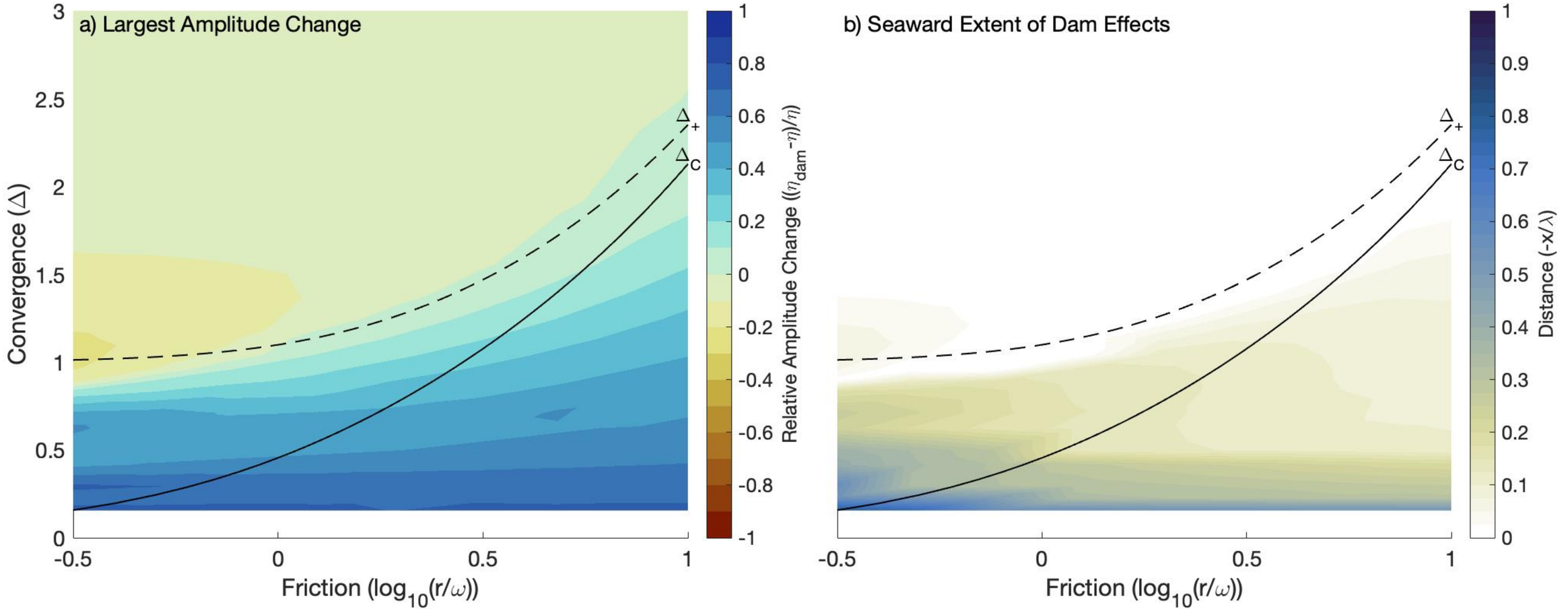
a) Largest Amplitude Change
b) Seaward Extent of Dam Effects
Convergence (Δ)
Friction (log10(r/ω))
Relative Amplitude Change ((ηdam−η)/η)
Distance (-x/λ)
Δ+
Δc
3
2.5
2
1.5
1
0.5
0
-0.5
0
0.5
1
0.8
0.6
0.4
0.2
-0.2
-0.4
-0.6
-0.8
-1
0.9
0.7
0.3
0.1